Magnetic Resonance Imaging 61 (2019) 41–65

Contents lists available at ScienceDirect

Magnetic Resonance Imaging

journal homepage: www.elsevier.com/locate/mri

Original contribution

A multi-objective optimization approach for brain MRI segmentation using fuzzy entropy clustering and region-based active contour methods

Thuy Xuan Pham, Patrick Siarry*, Hamouche Oulhadj

Laboratory Images, Signals, and Intelligent Systems (LiSSi), University Paris-Est Créteil, 94400 Vitry sur Seine, France

ARTICLE INFO

Keywords:
Image segmentation
Multi-objective particle swarm optimization
Kernelized fuzzy entropy clustering
Local and global region-based active contour
Magnetic resonance imaging

ABSTRACT

In this paper, we present a new multi-objective optimization approach for segmentation of Magnetic Resonance Imaging (MRI) of the human brain. The proposed algorithm not only takes advantages but also solves major drawbacks of two well-known complementary techniques, called fuzzy entropy clustering method and region-based active contour method, using multi-objective particle swarm optimization (MOPSO) approach. In order to obtain accurate segmentation results, firstly, two fitness functions with independent characteristics, compactness and separation, are derived from kernelized fuzzy entropy clustering with local spatial information and bias correction (KFECSB) and a novel adaptive energy weight combined with global and local fitting energy active contour (AWGLAC) model. Then, they are simultaneously optimized to finally produce a set of non-dominated solutions, from which $\mathscr{L}_2$-metric method is used to select the best trade-off solution. Our algorithm is both verified and compared with other state-of-the-art methods using simulated MR images and real MR images from the McConnell Brain Imaging Center (BrainWeb) and the Internet Brain Segmentation Repository (IBSR), respectively. The experimental results demonstrate that the proposed technique achieves superior segmentation performance in terms of accuracy and robustness.

1. Introduction

Image segmentation is the process of partitioning an image space into non-overlapped meaningful homogeneous regions or objects, according to given quantitative criteria: gray level, color, texture or combination of them [1]. For medical image analysis, the success of an image analysis system depends heavily on the quality of segmentation. We can find it in many real-life applications, for instance, in neurodegenerative disorders such as Alzheimer's disease, in movement disorders such as Parkinson's or Parkinson related syndrome, in congential brain malformations or perinatal brain damage, or in post-traumatic syndrome. However, the input MR brain images, which contain complex structures, are inherently noisy and often corrupted by intensity non-uniformity (INU) artifact due to various factors such as partial variations in illumination or radio frequency coil in image acquisition devices [2]. As a result, the automatic and accurate segmentation of MR images into different tissue classes, especially gray matter (GM), white matter (WM) and cerebrospinal fluid (CSF), remains a difficult task.

In order to achieve accurate segmented results, many segmentation techniques have been developed over many years and reported in the literature [3–5]. Their categorization is based on goals and specific aspects of data processing involved. Among those, fuzzy clustering and region-based active contours have been proved as the effective methods to produce segmented images. However, in both approaches, the image segmentation problem is formulated as an optimization problem, in which the energy fitting functions are non-convex and non-unique in nature and may have several local minimum points [6,7]. Therefore, besides dealing with the presence of noise and INU artifact, these methods suffer from the problem of getting trapped into the first local minimum they encounter when using the gradient descent search method [8].

Fuzzy clustering approach is one of the most widely used and studied methods in image segmentation because of its simplicity and applicability [9]. To cope with its challenges, many advanced methods have been proposed [10–14]. For instance, Namburu et al. [13] proposed a hybrid segmentation algorithm based on soft sets, namely soft fuzzy rough c-means, to extract the regions of gray matter, white matter and cerebrospinal fluid from MR brain image with bias field correction. Recently, we proposed a method [15] to handle the problem of trapping into local minimum and to overcome the presence of noise and INU artifact. The proposed method uses particle swarm optimization (PSO) algorithm and takes into account local partial information and bias field correction in kernelization. On the other side, the region-based active contour methods also have been extensively employed in medical

* Corresponding author.
E-mail addresses: thuy.pham@univ-paris-est.fr (T.X. Pham), siarry@u-pec.fr (P. Siarry), oulhadj@u-pec.fr (H. Oulhadj).

https://doi.org/10.1016/j.mri.2019.05.009
Received 5 June 2018; Received in revised form 16 April 2019; Accepted 4 May 2019

image segmentation [16,17]. For example, in [18–22], several methods have been proposed to overcome the problem of noise and INU artifact in segmentation of MR images. In [23], to avoid convergence to local minima in Chan-Vese (C-V) [24] model, the authors used the PSO algorithm to minimize the fitting energy function. These algorithms can produce promising segmentation results, but they only treat the image segmentation problem with a single criterion, which is insufficient for dealing with the different properties of the images. In other words, using the single objective is only dedicated to exploring a subset of search space and cannot model all the geometric properties of segmentation solution. Simultaneous optimization of multiple segmentation criteria will help developers to cope with several characteristics of partitioning, lead to higher quality solutions and increase the robustness towards the different data properties. Motivated by this, in the present work, we propose a new method that integrates the advantages of both methods, and at the same time, solves their current limitations by using multi-objective particle swarm optimization approach based on novel fitness functions.

The formulation of image segmentation problem posed as one of multi-objective optimization (MOO) problems and solved by metaheuristics has been successfully used [25]. Mukhopadhyay et al. [26,27] proposed methods using cluster validity measures or their variants as objective functions and genetic algorithms (GA) as the underlying multi-objective framework. These methods have an advantage that they can automatically evolve the number of clusters/regions. In the same direction [28,29], the authors introduced the non-local spatial information derived from the image into fitness functions and the Shapley value concept in selecting the best solution, respectively, to improve the segmentation results. Saha and Bandyopadhyay [30] proposed a method that uses the archived multi-objective simulated annealing (AMOSA) to simultaneously optimize two cluster validity indices, XB-index and Sym-index, for segmentation of MR brain images. In [31], to achieve a trade-off between preserving image details and restraining noise for image segmentation, the multi-objective evolutionary algorithm with decomposition (MOEA/D) is used to optimize FCM objective function and the other objective function designed by local information to restrain noise. In [32], Benaichouche et al. used a MOPSO algorithm to optimize two complementary criteria, which are based on the spatial fuzzy c-means (FCM) clustering measure and its following results. Here, instead of choosing the final solution in a set of Pareto front solutions, they proposed a method that combines all solutions to get a better segmentation.

Choosing appropriate criteria to produce better segmentation results is a key problem in image segmentation. The previous works mentioned above only consider cluster validity indices or their variants as objective functions. To the best of our knowledge, most recent works do not take into account the benefit of a criterion that comes from the other approaches like such active contours implemented in level set framework. In addition, PSO is a population-based stochastic optimization technique regarded as a global search strategy, originally introduced by Eberhart and Kennedy [33]. Compared with other metaheuristic algorithms such as GA, PSO has the advantages of simplicity, few parameter configurations, global exploration, adapted ability to some complex and continuous variable problems, and fast convergence. With the study of the MOPSO algorithms for problems of data clustering in general, several works have been proposed [34,35]. However, applying these algorithms to MOO clustering of image segmentation, particularly segmentation of MR brain images, needs to be further explored [25].

To achieve more accurate results, we propose in this paper a new method for brain MRI image segmentation, which takes advantages of both fuzzy clustering and region-based active contour methods, and simultaneously solves their main problems: (i) sensitivity to noise and INU artifact; (ii) trapping into local minima and dependency on initialization. Segmentation is solved within a MOO process using an improved variant of the MOPSO algorithms based on two independent objective functions and a decision maker. The first one is kernelized fuzzy entropy clustering with local spatial information and bias correction, which is taken from our previous work [15]. The second criterion is the adaptive energy weight global and local fitting energy active contour (AWGLAC) model, which is a novel model designed by using region-based active contour models with an adaptive mechanism for energy elements. Moreover, in both objective functions, the local spatial information and the bias correction are taken into account to cope with noise and INU artifact. The proposed MOPSO algorithm is a variant of the MOPSO algorithm introduced by Sierra and Coello [36] with advanced concepts in updating control parameters, and selections of the personal best and global best proposed in [35,37,38] to improve the search ability and quality of solutions. The output is a set of non-dominated Pareto optimal solutions, from which the $\mathscr{L}_2$-metric method is used to select the final one [39]. To validate the effectiveness of the proposed algorithm, we evaluate it on both simulated and real MR images from BrainWeb [40] and IBSR database,[1] respectively. The results are reported and compared with other recent segmentation methods in the literature.

The rest of the paper is organized as follows. The problem formulation is described in Section 2. The MOPSO fundamental and advanced concepts to improve the search ability and the quality of solutions are presented in Section 3. The description of the proposed method, using MOPSO approach and decision-making process for MR brain image segmentation is given in Section 4. The performance of our method is evaluated and compared with a set of algorithms from the literature in Section 5. Some discussions of choosing parameters and complexity analysis are represented in Section 6. Finally, in Section 7, we draw the conclusion of this work.

2. Problem formulation

2.1. Image model and problem formulation

There are several models of MR image formation in the literature [16]. Generally, they are based on assumptions that intensity inhomogeneity varies slowly over the entire image domain that otherwise would be constant for the same tissue type. In addition, the intensity inhomogeneity can be in multiplicative or additive types. Here, the multiplicative model is used since it is consistent with the inhomogeneous sensitivity of the reception coil. Noise in the image can be approximated by Gaussian probability distribution and is independent of the intensity inhomogeneity field. Furthermore, Huang and Zeng [21] also assume that there is a difference between the measured image and the traditionally approximated models in the local region. The difference is also independent of the intensity inhomogeneity and noise. Accordingly, an acquired MR image can be modelled as:

$$(I_j)_N = (I_j^{\mathrm{t}})_N (b_j)_N + (d_j)_N + (n_j)_N \tag{1}$$

where I_j is the measured intensity of the j^{th} MR pixel; I_j^{t} is the true intensity value approximated by a constant x_i^{c} for all pixel in the i^{th} tissue; b_j is the unknown smoothly varying biasfield, d_j is the local difference between the measured image and the traditionally approximated model, n_j is an additive zero-mean Gaussian noise with relatively small variance at the j^{th} pixel, and N is the number of pixels in the MR image.

In this work, we consider Eq. (1) as a decomposition of the MR image into four components: $(I_j^{\mathrm{t}})_N$, $(b_j)_N$, $(d_j)_N$, and $(n_j)_N$. From this, we formulate the image segmentation problem as a MMO problem and a decision-making process of finding optimal values of these components with a view of an image as a function I: $\Omega \rightarrow \Re$ on a continuous domain Ω.

Note that through the assumption of dependence between four

[1] http://www.nitrc.org/projects/ibsr/

components is not always satisfied, it is essential to examine our segmentation problem ushered in a computationally tractable form.

2.2. Goal and proposed solution

The objective is to segment the MR image in an unsupervised way with accurate results. To achieve this, the problem of MR image segmentation is formulated within a MOPSO framework and a decision-making process to simultaneously estimate the true image with several segments and the bias field. The MOO approach to the problem is motivated by seeking two important properties in segmented images: compactness and separation, from two complementary approaches named fuzzy clustering and region-based active contours. Particularly, the first fitness function, which is taken from our previous work [15], called kernelized fuzzy entropy clustering with local spatial information and bias correction, will have the purpose of minimizing the variation or scattering of the data within a particular tissue (compactness). In addition, the second fitness function is a novel one developed by combining local and global region-based active contour models with adaptive weight energy mechanism named adaptive energy weight local and global fitting energy active contour model. This objective will try to isolate the clusters/regions from each other (separation). Furthermore, the local spatial information and the bias correction are considered in both fitness functions to deal with noise and INU artifact. The output of the MOO algorithm is a set of non-dominated Pareto optimal solutions, in which certain solution is not possible to improve one objective without worsening another. Then, the $\mathscr{L}_2$-metric method is used to find final one with the best trade-off between the two objectives.

3. Multi-objective particle swarm optimization algorithm

3.1. Basic principles of PSO

Eberhart and Kennedy [33] originally proposed the PSO algorithm, which is inspired by social behaviour of bird flocking and fish schooling, for optimization problem. Similar to other evolutionary algorithms such as GA, PSO is a population based stochastic optimization algorithm and regarded as a global search strategy. However, many studies show that traditional PSO algorithms may easily be trapped into local suboptimal solutions. Several approaches [41,42] in literature have been proposed to overcome the problem. In PSO, each individual, which is considered as a potential solution to the optimization problem (called *particle*), of a given population (called *swarm*) can profit from the previous experiences of all other individuals from the same population. Through the search process in the solution space, each particle will adjust its velocity and position according to its own flying experiences as well as from the others in the swarm.

Let us consider a swarm of size *Np*. Each particle containing *L* elements, denoted by *i*, has a position vector $\mathrm{X_i} = (x_{i1}, x_{i2}, \dots, x_{iL})$ and a velocity vector $\mathrm{V_i} = (v_{i1}, v_{i2}, \dots, v_{iL})$, its own best position *pBest* found so far, and interacts with neighbouring particles through the best position *gBest* discovered in the neighbourhood so far. The position optimality is measured by means of one or more fitness functions defined in relation to the optimization problem. At iteration k^{th} in the search process, each particle is moved according to Eqs. (2) and (3):

$$\mathrm{V_i}(k+1) = w\mathrm{V_i}(k) + c_1 r_1 [pBest(k) - \mathrm{X_i}(k)] + c_2 r_2 [gBest(k) - \mathrm{X_i}(k)] \tag{2}$$

$$\mathrm{X_i}(k+1) = \mathrm{X_i}(k) + \mathrm{V_i}(k+1) \tag{3}$$

where r_1 and r_2 are random variables, uniformly distributed in $[0,1]$ to provide stochastic weighting of the different components participating in the velocity. c_1 and c_2 are acceleration coefficients that scale the influence of the cognitive and social components, respectively, and w is inertia weight.

There are two basic criteria for assessing the performance of PSO algorithm, namely, the convergence and the ability to find global optima. To optimize both criteria, keeping balance between global exploration and local exploitation is crucial.

3.2. Multi-objective particle swarm optimization algorithm

From a mathematical viewpoint, a general MOO problem can be formulated as follows:

$$\text{minimize:}\quad \mathcal{F}(\boldsymbol{x}) = (f_1(\boldsymbol{x}), f_2(\boldsymbol{x}), \dots, f_m(\boldsymbol{x}))^T$$
$$\text{subject to}\quad \begin{cases} g_j(\boldsymbol{x}) \geq 0, & j = 1, \cdots, J \\ h_k(\boldsymbol{x}) = 0, & k = 1, \cdots, K \end{cases} \tag{4}$$

where J and K are the numbers of inequality and equality constraints, respectively. $\boldsymbol{x} = (x_1, x_2, \dots, x_L)$ is a L-dimensional candidate solution in search space Ω. The mapping function Φ: $ga \rightarrow \Re^m$ defines m objective functions ($f_i(\boldsymbol{x})$, $i = 1, \dots, m$) and $\Re^m$ is called the objective space.

The solving of a MOO problem relies on a crucial concept, which is that of dominance. A decision vector $\boldsymbol{x_p} = (x_{p1}, x_{p2}, \dots, x_{pL})$ is said to strictly dominate another decision vector $\boldsymbol{x_q} = (x_{q1}, x_{q2}, \dots, x_{qL})$, donated by $\boldsymbol{x_p} \prec \boldsymbol{x_q}$. If the following conditions are met, one can say that $\boldsymbol{x_p}$ dominates $\boldsymbol{x_q}$ or $\boldsymbol{x_p}$ is better than $\boldsymbol{x_q}$:

$$\forall\, i: f_i(\boldsymbol{x_p}) \leq f_i(\boldsymbol{x_q}) \quad \text{and} \quad \exists\, j: f_j(\boldsymbol{x_p}) < f_j(\boldsymbol{x_q}) \tag{5}$$

where $i = 1, \dots, m$; $j = 1, \dots, m$. In MOO, when a solution is not dominated by any others, it is referred to as a Pareto optimal solution. The latter is said to be non-dominated, and the set of all non-dominated solutions forms the *Pareto front* of optimal solutions.

In MOO, each particle can have several non-dominant *pBest*. The swarm can also have several non-dominant *gBest*. As a result, extending PSO to MOO problems raises three fundamental questions [43]:

(i_1) How to select the *pBest* for each particle and the *gBest* for the swarm to give preference to non-dominated solutions?

(i_2) How to retain the non-dominated solutions found during the search process so that the solutions are non-dominated with respect to all the past populations, not only to the current one?

(i_3) How to maintain diversity in the swarm in order to avoid convergence towards a single solution?

For the image segmentation problem, several MOPSO-based approaches have been proposed in the literature [32,44,45]. However, previous studies have some limitations. Firstly, they do not take into account the distribution of solutions in the Pareto front, which have a unique feature in multi-objective clustering problems, to select the *gBest* [35]. Secondly, the *pBest* is given by comparing the present solution with the current *pBest*, and it replaces the *pBest* only if it dominates that solution, which may cause a lack of diversity of the algorithm. In addition, the flight parameters ($w, c_1,$ and c_2) are fixed, which comes from an experimentally exhausted process.

In this work, the approach proposed by Sierra and Coello [36] is considered as a basic MOPSO algorithm to develop. To improve the convergence and maintain diversity of the non-dominated solutions, we utilize the state of the art in MOPSO developments, particularly in the selection of *gBest*, *pBest*, and updating flight parameters. The procedure of improved MOPSO algorithm is summarized in Algorithm 2.

Note that, the crowding distance is calculated by using the procedure proposed by Kalyanmoy Deb et al. [46], which is described in Algorithm 1.

Algorithm 1. Crowding distance procedure.

```
crowdingDist (gA(t))
    inputs : The non-dominated solutions with size l in the gA(t)
    output: The distance corresponded to each solution, Dist
    foreach solution (i) do
        Set Dist[i] = 0;
    foreach objective (m) do
        Sort objective values;
        Assign Dist[1] = Dist[l] = ∞;
        for i = 2  to  (l − 1) do
            Dist[i] = Dist[i] + (gA(i + 1)_m − gA(i − 1)_m)/(f_m^max − f_m^min);
```

Here, $gA(i)_m$ refers to the m^{th} objective function value of the i^{th} individual in the global archive $gA(t)$ and parameters f_m^{max} and f_m^{min} are the maximum and minimum values of the m^{th} objective function, respectively.

Furthermore, the hypercubes in this work are currently built using an adaptive grid [47]. At each iteration, the objective space is divided using a grid so that the crowding of the solutions is measured using the crowding distance in the objective space within the grid. As a result, solutions at the highly populated cells can be removed or replaced to reduce computational overhead and overcome the problem of size limitation of the storing archives.

3.2.1. Global best selection mechanism

The selection of *gBest* is based on leader selection strategy of whole process proposed by Gong et al. [35], which makes MOPSO algorithm avoid trapping in local optimum by considering the distribution of the Pareto set. The *gBest* is selected among the leftmost, rightmost, and middle solutions in the current Pareto front with certain selection probability (higher for the middle one, and smaller for the others). In their works, the middle solution is selected as follows:

$$fit_s = \arg\left\{\min\left\{\sum_{j=1}^{m}\overline{f}_{ij}\right\}\right\}, \text{ with } i = 1, \cdots, N_{r'}; \quad j = 1, \cdots, m. \tag{6}$$

where $N_{r'}$ and m are the numbers of non-dominated solutions and fitness functions, respectively. $\overline{f}_{ij}$ is the objective function value of the j^{th} fitness function of the i^{th} solution after normalization.

However, in our work, to enhance the trade-off property of the middle solution among the others, we select the middle one as follows:

$$fit_s = \arg\left\{\min\left\{\sqrt{\sum_{j=1}^{m}\overline{f}_{ij}^{2}}\right\}\right\}, \text{ with } i = 1, \cdots, N_{r'}; \quad j = 1, \cdots, m. \tag{7}$$

Note that, for the problem with two fitness functions, the middle solution, actually, is the closest one to the ideal solution which simultaneously has minimum fitness values.

To examine the impact and efficiency of this mechanism, we did a comparison with the original one (applying roulette wheel selection to choose one hypercube among those having more than one particle, then, randomly selecting a particle in the hypercube and considering it as the global best) in the MOPSO algorithm proposed by Sierra and Coello [36] in terms of DICE coefficient. The two mechanisms were tested on simulated MR images (slices 75, 85, 95, 105, 115 with 9% noise and 40% INU artifact downloaded from BrainWeb). From Table 1 and Fig. 1, it can be seen that the proposed strategy generally provides better segmentation results, which are about 0.39% in terms of DICE coefficient in average.

3.2.2. Personal best selection mechanism

In this paper, the "Diversity" strategy proposed by Branke and Mostaghim is used because of its improvement ability in maintaining diversity for MOPSO algorithm [37]. The *pBest* is stored in personal archive and updated in each generation. Among all the *pBest* solutions visited in the past, the one which has the largest minimum crowding distance to any others, is selected. In other words, one selects the most isolated solution from the others as the current *pBest* toforce the particle to explore the regions which are far from those in the population.

Table 1
The average values in terms of DICE coefficient obtained when doing simulated MR image segmentation by using different strategies for selecting the global best.

Strategies	Slices					Average
	75	85	95	105	115	
The original	0.9425	0.9410	0.9583	0.9684	0.9688	0.9558
Proposed	0.9459	0.9479	0.9610	0.9725	0.9714	**0.9597**

The value in bold indicates the best performance.

3.2.3. Flight parameter mechanism

To have a better global exploration of the search space, most of existing works on MOPSO show that (w, c_1) parameters should be large and c_2 should be small in the beginning stage of iterations. Then, towards the end of the algorithm, to promote a better local exploitation, (w, c_1) parameters should be small and c_2 should be large. In this work, the law of updating flight parameters $(w, c_1, \text{and } c_2)$ is adopted from Zhang et al.'s work [38], in which the w is fixed (equal to 0.4) and the (c_1, c_2) are modified as follows:

$$c_1(k+1) = 2.5 - 2.\,(k/K_{max}),\ c_2(k+1) = 0.5 + 2.\,(k/K_{max}) \tag{8}$$

where k and K_{max} are, respectively, the iteration numbers starting from one and maximum number of allowable iterations.

Algorithm 2. iMOPSO.

```
Initialization: Set k = 1; the maximum number of iterations K_max;
                initialize population, pBest and gBest in (pA(t),
                gA(t)) archives, respectively, with bounded size; set
                {w, c1, c2}; generate hypercubes as coordinate systems
Results       : Report results in the gA(t)
repeat
    Determine the gBest using the strategy in 3.2.1
    Determine the pBest using the strategy in 3.2.2
    Update the flight parameters using Eq.8
    Calculate X_i and V_i according to Eqs. (2) and (3)
    Do mutation as detailed in [36]
    Check boundary conditions in search space for X_i and V_i
    Calculate the fitness values
    Update and store non-dominated solutions in pA(t) and gA(t)
    Maintain gA(t) using crowding distance technique
    Update the contents in the hypercubes as detailed in [36]
until the stopping criteria are met
```

4. Proposed method

This section describes the proposed image segmentation method, which is based on iMOPSO approach and a decision-making process. Two fitness functions are used, KFECSB and AWGLAC. The results of the iMOPSO algorithm is a set of Pareto solutions. In other words, the iMOPSO algorithm provides solutions such that each one cannot be estimated as better compared to the others. To find the final solution, the $\mathscr{L}_2$-metric method is used as a decision-making process to select one among the others in the Pareto set. The technique is illustrated below in detail.

4.1. Preprocessing

In this stage, there are two issues that are considered. The first one is skull stripping and the second is image enhancement.

Skull stripping is crucial to study neuroimaging data. Several existing techniques, such as Brain Extraction Tool (BET), Brain Surface Extractor (BSE), ANALYZE 4.0 (The Biomedical Imaging Resource at

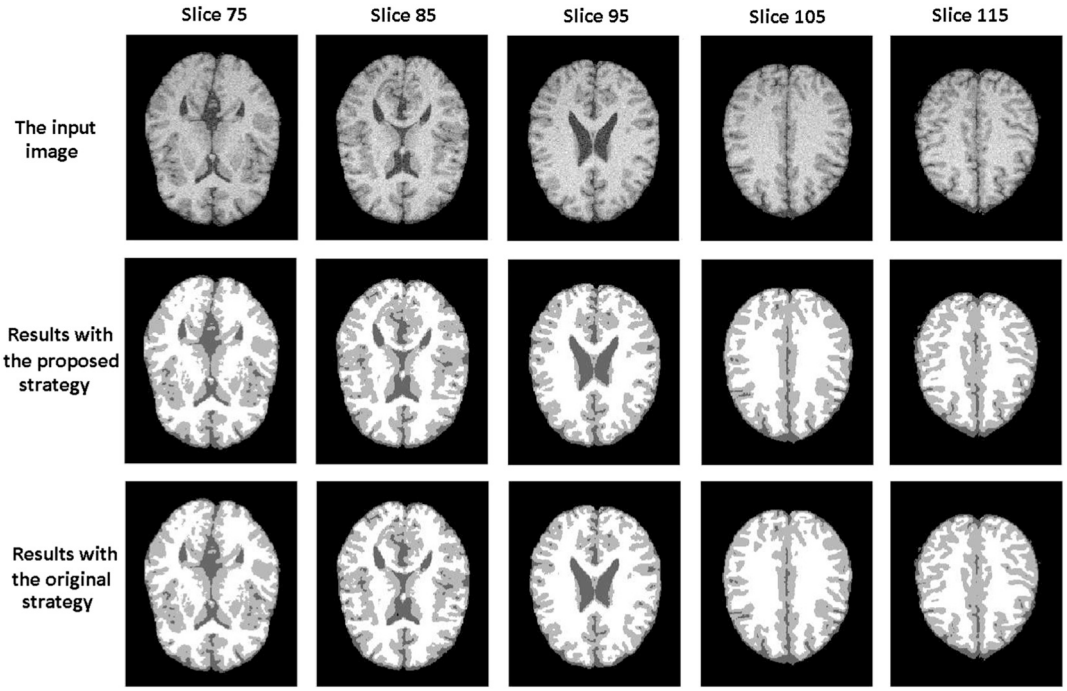

Fig. 1. Qualitative segmentation results using the proposed method with both T1-weighted skull brain image and skull-stripped brain image (slice 80 with 9% noise and 40% INU artifact).

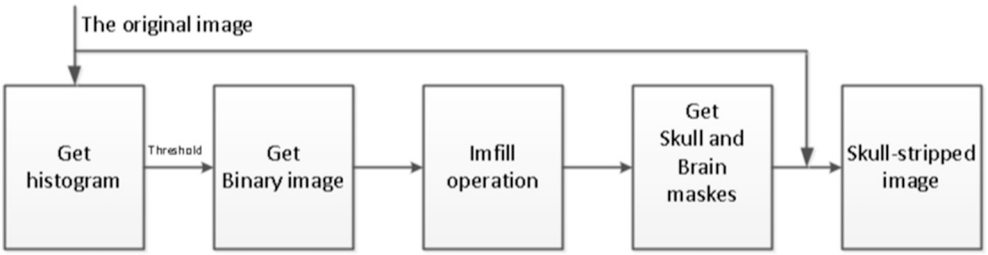

Fig. 2. Skull stripping procedure.

Mayo Clinic, Rochester, MN) and modified Region Growing tool (mRG), have been proposed to remove the skull and the background region from MRI [48]. In our work, the skull stripping algorithm, which is based on brain anatomy and image intensity, is illustrated in Fig. 2. First of all, the histogram of a given image is shown, from which a proper threshold is selected to get a binary image. Then, imfill operation is used to clean the binary image. By utilizing the solidity property and using morphological operations, the skull and brain regions are identified. Finally, the skull-stripped image is obtained by masking the original image with the brain region mask above.

Fig. 3 shows an example of segmentation results when applying the proposed method to segment brain MR image both with and without skull (slice 80 in BrainWeb dataset with 9% noise and 40% INU artifact). It is noticeable that the proposed method provides better qualitative segmentation results in case of the skull-stripped image. To clarify this issue, three different unsupervised criteria: Levine Nazif, Rosenberger Type I and Borsotti Q [49–51], were used for a quantitative performance evaluation. Table 2 also illustrates that better segmentation results can be achieved with input image without skull.

In addition, image enhancement is an essential step used in most applications of image analysis. Usually, brain images do not have good contrast and are corrupted by noise. To reduce the effect of these artifacts, in this work, the non-local algorithm for image denoising proposed by Antoni Buades et al. [52] was used. This algorithm not only decreases the noise in the image but also improves the local contrast of the image.

4.2. Particle representation

In this work, the particles are made up of real numbers which represent the coordinates of the cluster/region centers in the range of pixel values in the image. For N_p solutions with L distinct centers, there are in total (N_p. L) optimization variables that need to be encoded. For instance, the position of i^{th} solution in the population is encoded as: $\mathbf{X_i} = (x_{i1}, x_{i2}, \ldots, x_{iL})$. Here, x_{iq} $(q = 1, \cdots, Lt)$ represents the q^{th} cluster center among L centers of the i^{th} solution. In this way, the centers, $\mathbf{X} = (x_q^c)_L$, are obtained by decoding $\mathbf{X_i}$.

4.3. Segmentation criteria

The performance of a segmentation algorithm critically depends upon the criteria it tries to optimize simultaneously. We propose to jointly optimize two independent fitness functions to obtain both the complementary properties of segmented images: compactness and separation, simultaneously dealing with noise and INU artifact.

4.3.1. KFECSB

The first objective function is the kernelized fuzzy entropy

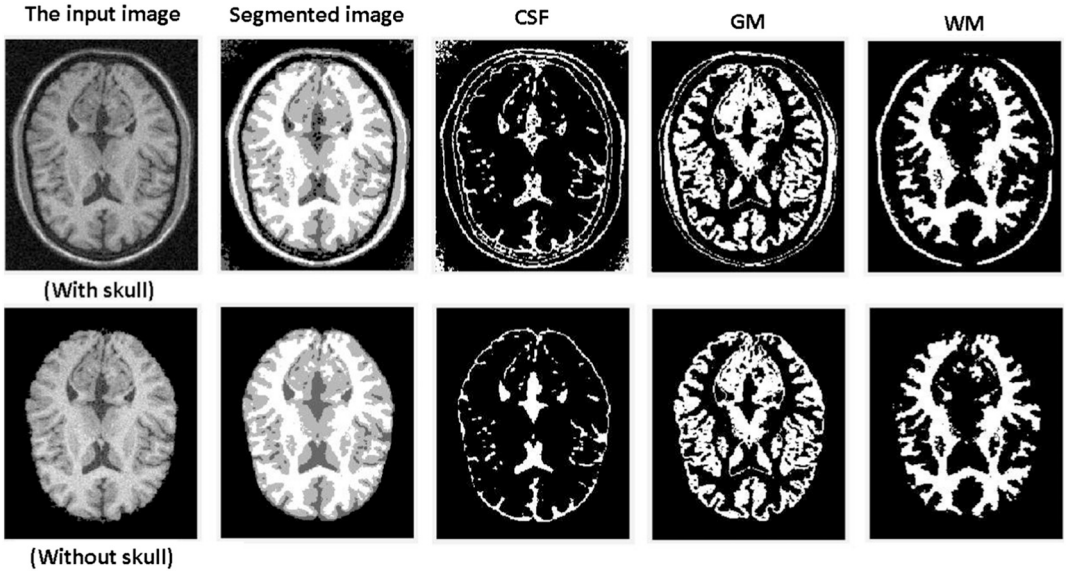

Fig. 3. Qualitative segmentation results using the proposed method with both T1-weighted skull brain image and skull-stripped brain image (slice 80 with 9% noise and 40% INU artifact).

Table 2
Quantitative segmentation results in terms of unsupervised criteria of the proposed method on slice 80 in simulated MR image dataset.

Types of images	Unsupervised criteria		
	Levine Nazif	Rosenberger Type I	Borsotti Q
With skull	0.5643	0.5728	0.0504
Without skull	**0.5911**	**0.6010**	**0.0448**

clustering with local spatial information and bias correction (KFECSB), taken from our previous work [15]. As brain MR images can be corrupted by different artifacts, a pixel at the boundary of two or more regions can easily induce classification errors under the greyness ambiguity or geometric blur that reduces the sharpness of the objects contours in the image. By using the fuzzy concept to consider each pixel belonging to several regions with different degrees, we can manage and overcome these difficulties more efficiently. Based on the assumptions in 2.1, we assume that the difference between a measured image and the approximated model in the local region is equal to zero. Let $I = (I_1, I_2, \ldots, I_N)$ be an image with N pixels, where I_j represents the intensity value of j^{th} pixel, the cost function is given by:

$$\mathcal{F}_{\mathrm{KFECSB}}(X, B, U) = \sum_{i=1}^{L}\sum_{j=1}^{N} u_{ij}(1 - K(I_j, x_i^c b_j)) + \frac{1}{\vartheta}\sum_{i=1}^{L}\sum_{j=1}^{N} u_{ij}\log(u_{ij}) + \eta \sum_{i=1}^{L}\sum_{j=1}^{N} u_{ij}(1 - K(I_j, x_i^c b_j)) \tag{9}$$

Satisfying the following conditions:

$$U \in \left\{ u_{ij} \in [0,1] \mid \sum_{i=1}^{L} u_{ij} = 1, \quad \forall j \quad \text{and} \quad 0 < \sum_{j=1}^{N} u_{ij}, \quad \forall i \right\} \tag{10}$$

where $X = (x_i^c)_L$ (with $1 < L < N$), $U = (u_{ij})_{L\times N}$ and $B = (b_j)_N$ are the set of L cluster prototypes, the partition matrix and the bias field estimation, respectively. $\bar{I} = (\bar{I}_j)_N$ is the median of the image I with window of size 3×3. $K(\cdot,\cdot)$ is the Gaussian kernel function, which is calculated by using Eq. (10)

$$K(I_j, x_i^c b_j) = e^{-\|I_j - x_i^c b_j\|^2/\sigma^2} \tag{11}$$

$$\text{with } \sigma^2 = \frac{\lambda}{N}\sum_{j=1}^{N}\|I_j - I_{mean}\|^2 \text{and } I_{mean} = \frac{1}{N}\sum_{j=1}^{N} I_j. \tag{12}$$

where λ is a constant fixed empirically.

By using the Lagrange multiplier method, the updates of the cluster centers, $X = (x_i^c)_L$, and the membership degrees, $U = (u_{ij})_{L\times N}$, are presented in Eqs. (13) and (14), respectively:

$$x_i^c = \frac{\sum_{j=1}^{N} u_{ij}[I_j.\, K(I_j, x_i^c b_j) + \eta.\, \bar{I}_j.\, K(\bar{I}_j, x_i^c b_j)]}{\sum_{j=1}^{N} b_j u_{ij}[K(I_j, x_i^c b_j) + eta.\, K(\bar{I}_j, x_i^c b_j)]} \tag{13}$$

$$u_{ij}^{-1} = \sum_{r=1}^{L} \frac{exp\left\{\frac{1}{\vartheta}[(1 - K(I_j, x_r^c b_j)) + \eta.\,(1 - K(\bar{I}_j, x_r^c b_j))]\right\}}{exp\left\{\frac{1}{\ddot{a}rtheta}[(1 - K(I_j, x_i^c b_j)) + \eta.\,(1 - K(\bar{I}_j, x_i^c b_j))]\right\}} \tag{14}$$

The bias field estimation of $B = (b_j)_N$, based on Li et al.'s work [20], is computed by using partition matrix, $U = (u_{ij})_{L\times N}$, and cluster centers, $\mathbf{X} = (x_i^c)_L$, as follows:

$$B = \left[\left(\sum_{i=1}^{L} G \times I \sum_{j=1}^{N} x_i^c u_{ij}\right)^{-1}\left(G \times G^T \sum_{j=1}^{N} (x_i^c)^2 u_{ij}\right)\right]^T G \tag{15}$$

where $G = (g_1, g_2, \ldots, g_H)^T$ is a set of 12 2D orthogonal three order Legendre polynomial functions.

4.3.2. AWGLAC

The second objective function is the adaptive energy weight combined with global and local fitting energy active contour models (AWGLAC). For MR brain images, there are more than two regions in a single slice, so we focus on the multiphase approach (3 or 4 regions) in this paper.

Vese and Chan proposed a multiphase model (MC-V) [8], called *global fitting energy* (GFE), which is used to extract 2^n objects with n level set functions. For $L = 4$ phases, let $\Phi = (\phi_1, i_2)$ be a vector level set function, and $\mathbf{C} = (C_1, C_2)$ be a set of closed curves expressed by the zero level set functions ϕ_i. $\{C_1 : \phi_1 = 0\} \cup \{C_2 : \phi_2 = 0\}$ partitions an image into four regions $\boldsymbol{\Omega} = (\Omega_1, \Omega_2, \Omega_3, \Omega_4)$, where the image domain $\Omega = \cup_{i=1}{}^{L}\Omega_i$ and $\Omega_i \cap \Omega_j = \oslash$ for $i \neq j$, with their average values $X = (x_i^c)_L$. In the level set framework [53], for the given image I(x) with point $x \in \Omega$, the energy functional of Φ can be formulated as:

$$\mathcal{F}^{\mathrm{GFE}}(\Phi, \mathrm{X}) = \sum_{i=1}^{L} \lambda_i \int_{\Omega} |\mathrm{I}(x) - x_i^{\mathrm{c}}|^2 M_i(\Phi(x))dx + \nu \mathcal{L}(\Phi) \tag{16}$$

where λ_i is positive constant which defines the weight of a term in the energy functional. ν is positive constant fixed empirically. $M_i(\Phi)$ is membership function representing the region Ω_i: $M_1(\Phi) = H_\epsilon(\phi_1)$. $H_\epsilon(\phi_2)$, $M_2(\Phi) = H_\epsilon(\phi_1)$. $(1 - H_\epsilon(\phi_2))$, $M_3(\Phi) = (1 - H_\epsilon(\phi_1))$. $H_\epsilon(\phi_2)$, and $M_4(\Phi) = (1 - H_\epsilon(\phi_1))$. $(1 - H_\epsilon(\phi_2))$, where $H_\epsilon(s) = \frac{1}{2}\left(1 + \frac{2}{\pi}\arctan\left(\frac{s}{\epsilon}\right)\right)$ with positive constant ϵ, is a smooth version of Heaviside function. $\mathcal{L}(\Phi)$ is a regularization term that computes the arc length of the zero level set contours of Φ and serves to smooth them during evolution, defined as follows:

$$\mathcal{L}(\Phi) = \int_{\Omega} |\nabla H_\epsilon(\phi_1(x))|dx + \int_{\Omega} |\nabla H_\epsilon(\phi_2(x))|dx \tag{17}$$

By minimizing Eq. (15) with respect to X and Φ, the segmented image is obtained as follows:

$$\mathbf{I}_{\mathrm{seg}} = \sum_{i=1}^{L} x_i^{\mathrm{c}} M_i(\mathbf{\Phi}) \tag{18}$$

Li et al. [22] pointed out that the energy weight parameters (λ_i) in the energy functional (16) are important and impact on the segmentation accuracy, especially when the areas of the objects and background are significantly different. They argue that each object should have the same contribution to the energy functional (16) and it would not be dependent on the others. Hence, to cope with this problem, the authors proposed adaptive energy weight functions to configure (λ_i) as illustrated as follows:

$$\lambda_i^{(k)} = f_i(\Phi^{(k)}) = \frac{size(I)}{Area(\Omega_i^{(k)})} = \frac{N}{Area(\Omega_i^{(k)})}$$
$$\text{with} \quad \mathrm{Area}(\Omega_i^{(k)}) = \int_{\Omega} M_i(\Phi^{(k)}(x))dx \tag{19}$$

where $\lambda_i^{(k)}$, $\mathrm{Area}(\Omega_i^{(k)})$, and $\Phi^{(k)}(x)$ are the energy weight, the area, and level set functions in the k^{th} iteration of the i^{th} region.

It is clear that the energy functional (16) does not take into account local partial information and thus is unable to deal with INU artifact. Inspired from the work of Li et al. [18], Huang and Zeng [21] proposed the model which is better in approximating the measured image and simultaneously solves the problem of intensity inhomogeneity by incorporating the local difference information between the acquired image and Li et al.'s estimate. The model based on local partial information of the image (called *local fitting energy* (LFE)) is given by:

$$\mathcal{F}^{\mathrm{LFE}}(\Phi, \mathrm{X}, \mathrm{B}, \mathrm{D}) = \nu \mathcal{L}(\Phi) + \mu \mathcal{P}(\Phi)$$
$$+ \int_{\Omega} \left(\sum_{i=1}^{L} \beta_i \int_{\Omega} K_\sigma(y - x)|\mathrm{I}(x) - b(y)x_i^{\mathrm{c}} - d(y)|^2 M_i(\Phi(x))dx \right) dy \tag{20}$$

where $\mathrm{X} = (x_i^{\mathrm{c}})_L$, $\mathrm{B} = (b_j)_N$, and $\mathrm{D} = (d_j)_N$ are the set of L mean intensity values, bias field estimation and the local difference, respectively. β_i is positive constant which defines the weight of different terms in the local energy functional. $K_\sigma(y - x)$ is a Gaussian kernel function (viewed as the weight at point y in local region of x) with window of size $(4\mathrm{w} + 1) \times (4\mathrm{w} + 1)$ and standard deviation σ, which is larger than w. μ is positive constant fixed empirically. $\mathcal{P}(\Phi)$ is a regularization term proposed by Li et al. [54] to eliminate the re-initialization step, which is defined as follows:

$$\mathcal{P}(\Phi) = \frac{1}{2}\int_{\Omega} (|\nabla\phi_1(x)| - 1)^2 dx + \frac{1}{2}\int_{\Omega} (|\nabla\phi_2(x)| - 1)^2 dx \tag{21}$$

Minimizing Eq. (20) with respect to X, Φ, B, and D, the segmented image is obtained by using Eq. (17).

By using local partial information, the work of Huang and Zeng is able to provide desirable segmentation results even in the presence of INU artifact. However, to some extent, the model is sensitive to initialization and hard to handle with the presence of noise. To solve this issue, several works [19,55–57] have been proposed by using the approach that consists in combining the global and local fitting energy functions. While the global information is used to improve the robustness in terms of noise and initialization (sometimes, it also maintains the boundary details [56]), the local information is considered to deal with INU artifact occurred in the given image. However, even most of the previous works assume that the energy weights associated with each region are fixed (equal to 1), this is not true as pointed out by Li et al. [22]. Moreover, tuning simultaneously several parameters in the combining models is a tedious work.

In this work, with the same approach, which uses both the global and local fitting energy functions, we propose a novel region-based active contour model with adaptive weights described as follows:

$$\mathcal{F}_{\mathrm{AWGLAC}}(\Phi, \mathrm{X}, \mathrm{B}, \mathrm{D}) = \omega \cdot \sum_{i=1}^{L} \lambda_i \int_{\Omega} |\mathrm{I}(x) - x_i^{\mathrm{c}}|^2 M_i(\Phi(x))dx + \mathcal{R}(\Phi)$$
$$+ (1 - \omega) \cdot \int_{\Omega} \left(\sum_{i=1}^{L} \beta_i \int_{\Omega} K_\sigma(y - x)|\mathrm{I}(x) - b(y)x_i^{\mathrm{c}} - d(y)|^2 M_i(\Phi(x))dx \right) dy \tag{22}$$

where $\omega = \left(\frac{1}{2\pi}\right)^2 \cdot (1 - h_{\mathrm{mean}})$ is a constant defined by the input image, which controls the influence of the GFE force and LFE force. Here, h_{mean} is the average of the local entropy with window of size 9×9 centered on each pixel in the whole image, which reflects the degree of the intensity inhomogeneous [57]. It is clear from the energy functional (22) that, when the presence of INU artifact (h_{mean}) in the given image is higher, the LFE force will be increased to deal with it. $\mathcal{R}(\Phi) = \nu\mathcal{L}(\Phi) + \mu\mathcal{P}(\Phi)$ is the combination of the regularization term and arc length term. The energy weight parameters (λ_i, β_i) are adaptively adjusted as follows:

$$\lambda_i^{(k)} = f_i^{\mathrm{g}}(\Phi) = \rho \cdot \frac{\min\{\mathrm{Area}(\Omega_i^{(k)})\}}{\mathrm{Area}(\Omega_i^{(k)})} \tag{23}$$

$$\beta_i^{(k)} = f_i^{\mathrm{l}}(\Phi) = \zeta \cdot \frac{\mathrm{Area}(\Omega_i^{(k)})}{\min\{\mathrm{Area}(\Omega_i^{(k)})\}}, \quad \text{with } i = 1, \cdots, L. \tag{24}$$

where (ρ, ζ) are scale parameters determined by experiments and $\mathrm{Area}(\Omega_i^{(k)})$ is defined as in Eq. (19).

With the definition of the energy weight parameters as in Eqs. (23) and (24), it is obvious that each object fairly contributes in the energy functional (controlled by $\lambda_i^{(k)}$) in the whole image. On the other hand, in local area the difference among regions is enhanced (controlled by $\beta_i^{(k)}$). Hence, in this way, by minimizing Eq. (21), we can obtain a better result of image segmentation.

Using the gradient descent method, the solution of $(\Phi, \mathrm{X}, \mathrm{B}, \mathrm{D})$ when we minimize Eq. (21) with respect to each of its variables, given the others in previous iteration, is achieved as follows.

For fixed B, D, and Φ, the optimal $\mathrm{X} = (x_i^{\mathrm{c}})_L$ that minimizes Eq. (22), is given by:

$$x_i^{\mathrm{c}} = \frac{\omega \cdot \lambda_i \int_{\Omega} I(x) M_i(\Phi)dx + (1 - \omega) \cdot \beta_i \int_{\Omega} (K_\sigma * B)(I(x) - D) M_i(\Phi)dx}{\omega \cdot \lambda_i \int_{\Omega} M_i(\Phi)dx + (1 - \omega) \cdot \beta_i \int_{\Omega} (K_\sigma * B^2) M_i(\Phi)dx} \tag{25}$$

Keeping X, B, and D fixed, and minimizing the energy functional $\mathcal{F}_{\mathrm{AWGLAC}}$ in Eq. (22) with respect to Φ, we can deduce the associated Euler-Lagrange equations for Φ. By introducing an artificial time variable $t \geq 0$, the gradient flow equation for updating Φ is as follows:

$$\frac{\partial\phi_l^{(k)}}{\partial t} = -\sum_{i=1}^{L} \frac{\partial M_i(\Phi^{(k)})}{\partial\phi_l^{(k)}} \cdot e_i^{(k)} + \nu \cdot \delta_\epsilon(\phi_l^{(k)}) \,\mathrm{div}\left(\frac{\nabla\phi_l^{(k)}}{|\nabla\phi_l^{(k)}|}\right) + \mu \cdot \left(\nabla^2\phi_l^{(k)} - \mathrm{div}\frac{\nabla\phi_l^{(k)}}{|\nabla\phi_l^{(k)}|}\right) \tag{26}$$

$$\phi_l^{(k+1)} = \phi_l^{(k)} + \triangle t \frac{\partial \phi_l^{(k)}}{\partial t} \tag{27}$$

with the initial and Neumann boundary conditions are defined by:

$$\phi_l(x,0) = \phi_l^{(0)}(x), \quad x \in \Omega \tag{28}$$

$$\frac{\partial \phi_l^{(k)}}{\partial \mathbf{n}} = 0, \quad x \in \partial\Omega \tag{29}$$

where $l = 1, 2$, and $\phi_l{}^{(0)}(x)$ is the initial level set l^{th} function. $\mathbf{n}$ denotes the exterior normal to the boundary $\partial\Omega$. $\triangle t$ is time step. $\delta_\epsilon(\phi_l{}^{(k)})$ is the Dirac delta function, which is the derivative of $H_\epsilon(\phi_l{}^{(k)})$: $\delta_\epsilon(s) = H_\epsilon{}'(s) = \frac{1}{\pi}\frac{\epsilon}{\epsilon^2+s^2}$. $e_i^{(k)}$ is a function defined as follows:

$$e_i^{(k)} = (1-\omega)\int_\Omega \beta_i^{(k)} K_\sigma(y-x)|\mathrm{I}(x) - b(y)x_i^c - d(y)|^2 dy + \omega\lambda_i^{(k)}|\mathrm{I}(x) - x_i^c|^2 \tag{30}$$

Similarly, we obtain the optimal B and D as follows:

$$\mathrm{B} = \frac{K_\sigma * ((I - D).\sum_{i=1}^{L} x_i^c.\, M_i(\Phi))}{K_\sigma * \sum_{i=1}^{L}(x_i^c)^2.\, M_i(\Phi)} \tag{31}$$

$$\mathrm{D} = \frac{K_\sigma * \sum_{i=1}^{L}(I - x_i^c.\, B) M_i(\Phi)}{K_\sigma * \sum_{i=1}^{L} M_i(\Phi)} \tag{32}$$

where '$*$' is the convolution operator.

To verify the effectiveness of the proposed model (22), we segment MR images using the PSO-based framework proposed by Mandal et al. [23], that we extended for multiphase case with the same termination conditions introduced in [56], for three fitness functions (16), (20), and (22), with default settings as in the literature. As a simple example, Fig. 4 shows the segmentation results for the different fitness functions when segmenting T1-weighted image (slice 97) with noise level of 9% and intensity inhomogeneity of 40%. It is clear that when using the energy functional (22) as a fitness function of the image segmentation problem, we can obtain superior results compared to the counterparts.

4.4. The optimum search process

In our work, the iMOPSO algorithm illustrated in Section 3 is used to find a set of Pareto solutions by minimizing the two fitness functions $\mathscr{F}_{\mathrm{KFECSB}}$ and $\mathscr{F}_{\mathrm{AWGLAC}}$. The MOO frameworkfor the image segmentation problem is summarized in Algorithm 3.

In the initialization, the population $(\mathrm{X_i})_{N_p}$ is generated randomly. Each individual $\mathbf{X_i} = (x_{i1}, x_{i2}, \ldots, x_{iL})$ is a L-dimension decision vector (with $L = 3$ or 4), where L is the number of cluster centroids. And then, the initial level set function associated with the solution $\Phi^{(0)}$ is configured by following some steps. First, the elements of the decision vector are sorted in ascending order, $(x_{i1}', x_{i2}', \ldots, x_{i4}')$. Next, the $\Phi^{(0)}$ is determined as explained as follows:

If the number of regions is three ($L = 3$), where $M_1(\Phi) = H_\epsilon(\phi_1)$. $H_\epsilon(\phi_2)$, $M_2(\Phi) = H_\epsilon(\phi_1)$. $(1 - H_\epsilon(\phi_2))$, and $M_3(\Phi) = 1 - H_{silon}(\phi_1)$, the $\Phi^{(0)}$ are initialized as:

$$\phi_1^{(0)} = \alpha\bullet\mathrm{sign}(\mathrm{I} > x_{i1}') \quad \text{and} \quad \phi_2^{(0)} = \alpha\bullet\mathrm{sign}(\mathrm{I} > x_{i2}') \tag{33}$$

If the number of regions is four ($L = 4$), the $\Phi^{(0)}$ are initialized as:

$$\phi_1^{(0)} = \alpha\bullet\mathrm{sign}(\mathrm{I} < x_{i3}') \quad \text{and} \quad \phi_2^{(0)} = \alpha\bullet\mathrm{sign}((\mathrm{I} > x_{i2}') \cup (\mathrm{I} < x_{i4}')) \tag{34}$$

where α is a constant, we set equal to 2, and I is the input image.

To make sure that all particles are moving within the search space, the boundary conditions for their velocities and positions ($\mathrm{V_i}$, $\mathrm{X_i}$) are limited as follows:

$$v_{ij}(k+1) = \begin{cases} v_{max}, & \text{if } v_{ij}(k+1) > v_{max} \\ v_{min}, & \text{if } v_{ij}(k+1) < v_{min} \\ +\, v_{ij}(k+1), & \text{otherwise} \end{cases} \tag{35}$$

$$x_{ij}(k+1) = \begin{cases} x_{max}, & \text{if } x_{ij}(k+1) > x_{max} \\ x_{min}, & \text{if } x_{ij}(k+1) < x_{min} \\ +\, x_{ij}(k+1), & \text{otherwise} \end{cases} \tag{36}$$

where v_{min} and v_{max} are the smallest and largest allowable step sizes in any dimension ($v_{min} = -v_{max} = -1$ is set in this paper); and $\{x_{min}, x_{max}\}$ are the bounds of the search space in each dimension. Actually, they are the minimum and maximum of the intensity value of the input image.

Furthermore, to provide a flexible choice for user and a resource for further post-processing stage, maintaining the external archive gA(t), where stores non-dominated solutions, includes both output information for fuzzy entropy clustering ($\mathbf{U}$, $\mathbf{B}^{\mathrm{fc}}$) and region-based active contour ($\mathbf{\Phi}$, $\mathbf{B}^{\mathrm{ac}}$) methods. However, in this work we get segmented images by using the output of fuzzy entropy clustering method.

The terminating condition in Algorithm 3 is the maximum number of iterations. When ($k > K_{max}$) is reached, the algorithm is immediately stopped.

4.5. Decision making

After getting a Pareto set, one solution must be selected, and consequently, we are facing a multi-criteria decision making (MCDM) problem. We also know that these solutions share the property of

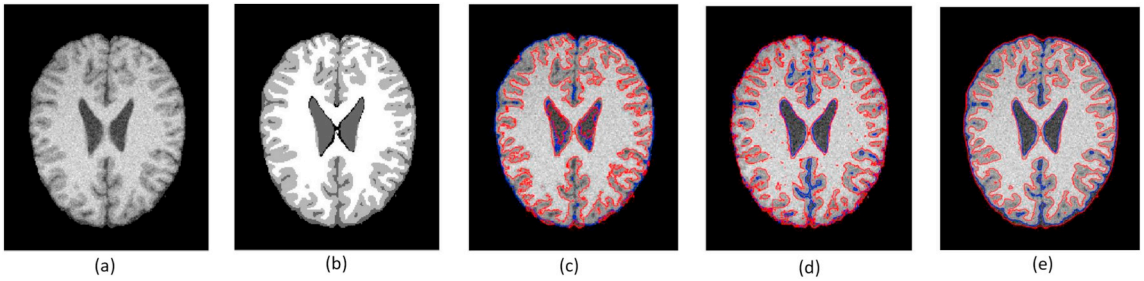

Fig. 4. Segmentation results of a simulated MR brain image (slice 97) by the different objective functions: (a) the original image after skull tripping; (b) the ground truth image; (c) the segmented result with the energy functional (16); (d) the segmented result with the energy functional (20); (e) the output using the proposed objective function.

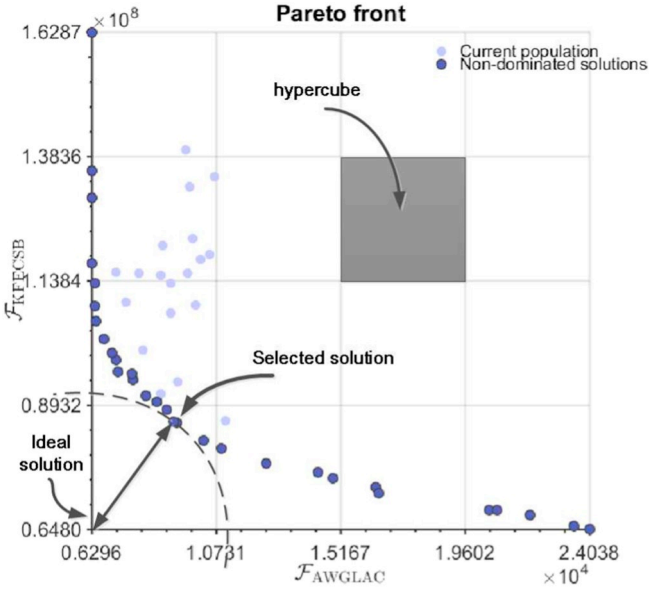

Fig. 5. $\mathscr{L}_2$-metric method for selecting final solution in a typical Pareto front: results for a real MR image (slice 35) using the proposed MOPSO approach.

improving the value of one objective function but leading to a degradation of the other one. Hence, a decision is required to make a trade-off while giving a choice. Several methods have been proposed to determine which solution in the Pareto set should be chosen [39,58]. Here, we use a distance-based technique, called $\mathscr{L}_2$-metric method, proposed by Padhye and Deb [39]. The $\mathscr{L}_2$-metric method is based on the selection of the alternative that is the closest to the ideal solution. Specifically, first, each objective is normalized between [0, 1]. Then, the ideal point (solution) is constructed, which is the intersection point of lines passing through the top right and bottom left solutions of the Pareto front (Fig. 5). Euclidean distance ($\mathscr{L}_2$) of each point in non-dominated set is calculated from the ideal point and the one which has the smallest Euclidean distance will be chosen.

Note that, since experimental results for each fitness function (PSO-KFECSB and PSO-AWGLAC) as listed in Appendices B and C are comparable, the importance of each objective is evaluated equally ($w_{fe} = w_{ac} = 1$). However, for a certain image (if we know which one is better than the other), we can provide weights for each objective function when calculating the Euclidean distance, as follows:

$$\text{EuclideanDist} = \sqrt{w_{fe}.\ \text{norm}(\mathscr{F}_{\text{KFECSB}})^2 + w_{ac}.\ \text{norm}(\mathscr{F}_{\text{AWGLAC}})^2} \quad (37)$$

where w_{fe} and w_{ac} define the importance of the two objective functions, respectively.

5. Experimental results

5.1. Experimental setup

In this section, we empirically evaluate the performance of the proposed method. Particularly, the aim is to address the possibility of the proposed algorithm to effectively improve the performance in segmentation of MR brain images. To validate the effectiveness of our framework, the results are examined both qualitatively and quantitatively, and compared with those obtained from six state-of-the-art algorithms and a PSO based algorithm with the second objective function (22). They are current variants of FCM, named adaptively regularized kernel-based fuzzy C-means clustering (ARKFCM) [12] and FCM algorithm based on morphological reconstruction and membership filtering (FRFCM) [14], ~~and~~ the multiplicative intrinsic component optimization (MICO) [20] and the well-known region-based level set method, called LIC [18]. Additionally, ~~the well-known region-based level set method, called LIC [18], and~~the metaheuristic multilevel threshold with Markov random field (PSO-MRF) [59], the PSO based on global and local region-based active contour (PSO-AWGLAC) and our previous work, called PSO-KFECSB algorithm [15], are used. The algorithms' parameters setting is specified in Appendix A. All of the algorithms are implemented in MATLAB 2014b and executed with a computer with Intel Core i7 1.8 GHz CPU, 8 G RAM using Microsoft Windows 10.

Furthermore, from recommendations in similar context in the literature [15,18] and the trial-and-error method with experiments around those parameter values, we sorted out parameter values for the proposed algorithm as follows: swarm size $N_p = 30$, external archive of non-dominated solutions size $N_r = 30$, number of grids per dimension $N_g = 10$, maximum number of iterations $K_{max} = 200$ (180 for real MR images), and selection probabilities for the leftmost, rightmost, and middle solutions: 15 % , 15%, and 70%, respectively. For the first fitness function (9), $\mathscr{F}_{\text{KFECSB}}$, the values of ($\vartheta$, η, and λ) are 10, 2.5, and 1/9 [15], respectively. For the second fitness function (22), $\mathscr{F}_{\text{AWGLAC}}$, unless otherwise specified, we set $\epsilon = 3$, $\sigma = 5$, $\alpha = 2$, $\Delta t = 1$, and $\mu = 1$, as common values in the literature. Note that, due to the nature of active contour models, the weighting coefficients ν, ρ, and ζ are differently set for each type of image. The effect of the arc length parameter ν was useful and briefly discussed in [60,61]. In addition, depending on the level of noise and INU artifact, one can increase the value of ρ (for high level of intensity inhomogeneity), or ζ (for high level of noise), and vice versa.

Algorithm 3. iMOPSO-based image segmentation algorithm.

Initialization: Read the input image and determine the range of search space $[x_{min}, x_{max}]$; set the number of regions: L; set the number of iterations: $k = 1$ and K_{max}; initialize population: $(\mathbf{X_i})_{N_p}$; initialize level set functions: $(\phi_1^{(0)}, \phi_2^{(0)})$, for each particles; initialize flight parameters: $\{w, c_1, c_2\}$; set up parameters for the two fitness functions ($\mathcal{F}_{\text{KFECSB}}$ and $\mathcal{F}_{\text{AWGLAC}}$ as introduced in Eqs. (9) and (22)), then calculate fitness values for each particle; determine *pBest*, *gBest* and store in external pA(t) and gA(t) archives, respectively; generate hypercubes as coordinate systems

Results : Report results in the gA(t)

repeat

  for *each particle* **do**

1 Update *pBest*, *gBest* and the flight parameters $\{w, c_1, c_2\}$

2 Calculate $\mathbf{X_i}$ and $\mathbf{V_i}$ according to Eqs. (2) and (3)

3 Do mutation: generate new particles by implemeting mutation operator on a part of the population (This part is exactly the same as in [36])

4 Check boundary conditions in search space for $\mathbf{X_i}$ and $\mathbf{V_i}$

5 Evaluate fitness values for the $\mathcal{F}_{\text{KFECSB}}$ as following steps:

5.1 Estimate kernel distance K by using Eq. (11)

5.2 Estimate the partition matrix $\mathbf{U}$ by using Eq. (14)

5.3 Estimate the bias field correction $\mathbf{B}^{\text{fc}}$ by using Eq. (15)

5.4 Calculate the fitness values by using Eq. (9)

6 Evaluate fitness values for the $\mathcal{F}_{\text{AWGLAC}}$ according to following steps:

6.1 Estimate the mean intensity value, x_i^{ac}, using Eq. (25)

6.2 Evolve the level set functions $\mathbf{\Phi}$ by using Eq. (27)

6.3 Update energy weights (λ_i, β_i) by using Eqs. (23) and (24)

6.4 Estimate the bias field correction $\mathbf{B}^{\text{ac}}$ by using Eq. (31)

6.5 Estimate the difference $\mathbf{D}$ by using Eq. (32)

6.6 Calculate the fitness values by using Eq. (22)

7 Update and store non-dominated solutions in pA(t) and gA(t)

8 Maintain gA(t) using crowding distance technique

9 Update the contents in the hypercubes

until *the stopping criteria are met*

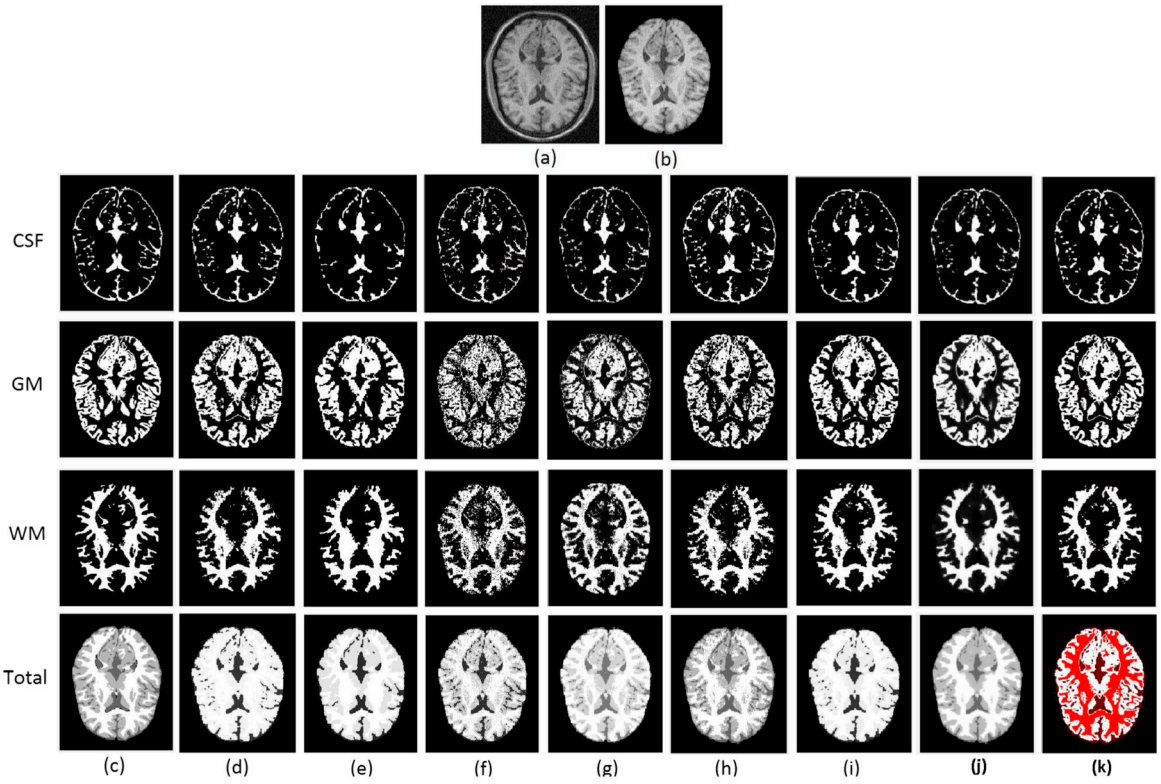

Fig. 6. Qualitative segmentation results of a simulated MR brain image (slice 80) with 9% noise and 40% INU artifact provided by the competing algorithms: (a) original image; (b) original image after skull stripping; (c) ground truth images; (d)ARKFCM results; (e) FRFCM results; (f) MICO results; (g) LIC results; (h) PSO-MRF results; (i) PSO-KFECSB results; (j) PSO-AWGLAC results; (k) the proposed method results.

5.2. Datasets

The MR images used in this study include both T1-weighted simulated and real 2D MRI brain images. For simulated MR images, they are downloaded from a well-known database: the BrainWeb from a McConnell Brain Imaging Center [40]. The size of the synthetic images is 181 × 217 and that of the voxels is 1 × 1 mm^2. On the other hand, real images are taken in the 20 normal MR brain data sets provided by the Center for Morphometric Analysis at Massachusetts General Hospital, which are available at http://www.nitrc.org/projects/ibsr/. The size of the images is 135 × 142 and that of the voxels is 1.171751 × 1.171751 mm^2.

Note that several image modalities used in medical imaging, such as Roentgen rays (X-rays), Magnetic Resonance Imaging (MRI), Ultrasound (US), Computed Tomography (CT) and Positron Emission Tomography (PET), each with its own advantages and disadvantages, have appeared over the years. This study focused on images produced by structural imaging techniques and satisfied assumptions mentioned in Section 2.1. As a result, images produced by the other techniques, functional imaging [62], such as PET, may not be suitable for our method.

5.3. Performance measures

Since the ground truth images are available in the datasets, for comparing quantitatively the performance, five performance measures are considered, which are: the Dice Similarity Coefficient (DICE), the Hausdorff distance (HD), the Jaccard index (JAC), the Accuracy (AC) and the Sensitivity (SI) [63–66]. These are defined below.

5.3.1. Dice coefficient

The Dice coefficient [63] (DICE) is an overlap-based metric which directly compares a segmented image (I_{seg}) with a ground truth image (I_{tr}) by measuring similarity between them. This metric is one of the most used measures in validating medical volume segmentations. Given an input image with N pixels $I = (I_1, I_2, \ldots, I_N)$, and its two partitions, $I_{seg} = (I_{seg1}, I_{seg2}, \cdots, I_{segN})$ (the segmented image) and $I_{tr} = (I_{tr1}, I_{tr2}, \cdots, I_{trN})$ (the ground truth image), there are four common cardinalities that reflect the overlap between the two partitions, namely the true positives (TP), the false positives (FP), the true negatives (TN), and the false negatives(FN). Then, the pair-wise overlap of the repeated segmentations is calculated using the DICE, which is defined by:

$$\mathrm{DICE}(I_{seg}, I_{tr}) = \frac{2.\ |I_{seg} \bigcap I_{tr}|}{|I_{seg}| + |I_{tr}|} = \frac{2.\ TP}{2.\ TP + FP + FN} \tag{38}$$

5.3.2. Hausdorff distance

The Hausdorff distance [64] (HD) is a distance-based metric which measures the dissimilarity between the segmented image (I_{seg}) and the ground truth image (I_{tr}). This is also a widely used metric, defined as

follows:

$$\mathrm{HD}(\mathrm{I}_{\mathrm{seg}}, \mathrm{I}_{\mathrm{tr}}) = \max\{h(\mathrm{I}_{\mathrm{seg}}, \mathrm{I}_{\mathrm{tr}}), h(\mathrm{I}_{\mathrm{seg}}, \mathrm{I}_{\mathrm{tr}})\} \tag{39}$$

where $h(\mathrm{I}_{\mathrm{seg}}, \mathrm{I}_{\mathrm{tr}})$ is called the directed Hausdorff distance given by:

$$h(\mathrm{I}_{\mathrm{seg}}, \mathrm{I}_{\mathrm{tr}}) = \max_{I_{\mathrm{seg}\,i} \in \mathrm{I}_{\mathrm{seg}}} \min_{I_{\mathrm{tri}} \in \mathrm{I}_{\mathrm{tr}}} \|I_{\mathrm{seg}\,i} - I_{\mathrm{tri}}\| \tag{40}$$

where $\|I_{\mathrm{seg}i} - I_{\mathrm{tri}}\|$ is the Euclidean distance between the intensity values of the $I_{\mathrm{seg}i}$ pixel and the I_{tri} pixel in the segmented and ground truth images, respectively.

5.3.3. Jaccard index

This is an overlap-based metric which directly compares a segmented image ($\mathrm{I}_{\mathrm{seg}}$) with a ground truth image (I_{tr}) by measuring similarity between them. A higher value indicates a better result. The Jaccard index is defined as follows:

$$\mathrm{JAC}(\mathrm{I}_{\mathrm{seg}}, \mathrm{I}_{\mathrm{tr}}) = \frac{|I_{seg} \bigcap I_{tr}|}{|I_{seg} \bigcup I_{tr}|} = \frac{TP}{TP + FP + FN} \tag{41}$$

From Eqs. (38) and (41), we can see that: DICE = 2 · JAC/(1 + JAC) and JAC = DICE/(2 − DICE) for any input. That means that both metrics measure the same aspects and provide the same system ranking.

5.3.4. Accuracy

This criterion determines how much the segmentation algorithm results match with the ground truth. It is defined as follows:

$$\mathrm{AC}(\mathrm{I}_{\mathrm{seg}}, \mathrm{I}_{\mathrm{tr}}) = \frac{TP + TN}{TP + TN + FP + FN} \tag{42}$$

5.3.5. Sensitivity

This criterion indicates true positivity and it is the probability that a pixel in segmented image belongs to a particular region. Definition of the criterion is given as follows:

$$\mathrm{SI}(\mathrm{I}_{\mathrm{seg}}, \mathrm{I}_{\mathrm{tr}}) = \frac{TP}{TP + FN} \tag{43}$$

Table 3
Average values in terms of five criteria (DICE, HD, JAC, AC, SI) on simulated MR brain images using different algorithms.

Methods	Regions	Performance criteria				
		DICE	HD	JAC	AC	SI
ARKFCM	CSF	0.9242	202.3333	0.8714	0.8770	0.9407
	GM	0.8842	126.5000	0.7993	0.8389	0.8722
	WM	0.9451	108.3333	0.8963	0.9251	0.9299
	Total	0.9062	80.5000	0.8373	0.9322	0.8932
FRFCM	CSF	0.9776	479.8333	0.9563	0.9607	0.9741
	GM	0.9241	124.6667	0.8589	0.8974	0.9289
	WM	0.9493	210.1667	0.9038	0.9324	0.9495
	Total	0.9415	81.0000	0.8901	0.9582	0.9402
MICO	CSF	0.9792	**184.5000**	0.9593	0.9638	**0.9826**[a]
	GM	0.8828	180.1667	0.7904	0.8392	0.8723
	WM	0.9041	187.6667	0.8250	0.8729	0.9135
	Total	0.9187	162.5000	0.8502	0.9420	0.9227
LIC	CSF	**0.9828**	195.1667	**0.9661**	**0.9697**	0.9748
	GM	0.8875	172.6667	0.7983	0.8443	0.8658
	WM	0.9018	182.6667	0.8214	0.8728	0.9324
	Total	0.9201	151.6667	0.8529	0.9428	0.9161
PSO-MRF	CSF	0.9658	214.0000	0.9350	0.9403	0.9800
	GM	0.9163	145.8333	0.8460	0.8863	0.9092
	WM	0.9425	136.8333	0.8915	0.9231	0.9409
	Total	0.9242	122.0000	0.8601	0.9438	0.9346
PSO-KFECSB	CSF	0.9797	224.0000	0.9634	0.9635	0.9691
	GM	**0.9414**	114.0000	**0.8924**	0.9203	0.9424
	WM	0.9641	78.1667	0.9308	0.9522	0.9694
	Total	0.9543	64.6667	0.9171	0.9664	0.9544
PSO-AWGLAC	CSF	0.9545	380.1667	0.9141	0.9157	0.9161
	GM	0.9112	180.1667	0.8384	0.8762	0.9068
	WM	0.9360	204.5000	0.8819	0.9159	0.9571
	Total	0.9147	167.0000	0.8442	0.9351	0.8826
Proposed	CSF	0.9819	234.5000	0.9645	0.9678	0.9719
	GM	0.9412	**105.5000**	0.8890	**0.9208**	**0.9467**
	WM	**0.9654**	**76.0000**	**0.9331**	**0.9539**	**0.9704**
	Total	**0.9575**	**53.3333**	**0.9187**	**0.9695**	**0.9551**

[a] The bold numerical values indicate the best performance.

5.4. Simulated MR brain images

In this section, simulated MR brain images from the BrainWeb are used for the purpose of performance evaluation. Each image is segmented into four regions: cerebro spinal fluid (CSF), gray matter (GM), white matter (WM), and the background. The rest of parameters is a set of the weighting coefficients ($\nu = 0.00015 * 255^2$, $\rho = 9$, and $\zeta = 0.1$).

To establish the performance of the proposed algorithm with respect to noise and INU artifact, experiments have been performed by considering images containing high level of noise and intensity inhomogeneity. Particularly, those are T1-weighted images with 9% noise and 40% INU artifact.

Fig. 6 shows the qualitative results of the segmentation of a T1-weighted image (slice 80) provided by different algorithms. This figure reveals that though the PSO-KFECSB, FRFCM and the proposed algorithm, among the existing methods, yield positive outcomes, those from the multi-objective approach are the best ones, reserving the correct details of the image in specific. Fig. 9 shows the qualitative results of the segmentation of five T1-weighted images (slices: 75, 80, 85, 95, 105, 115). In spite of artifact existence, it can be seen that the proposed algorithm achieves a high performance when segmenting simulated MR brain images. Hence, it can be concluded that our proposed algorithm provides qualitatively satisfactory results.

Table 3 shows the average values of ~~the Dice coefficient and Hausdorff distance~~five metrics of eight competing algorithms: ARKFCM, FRFCM, MICO, LIC, PSO-MRF, PSO-KFECSB, PSO-AWGLAC, and the proposed algorithm. Note that the details for numerical values when segmenting different images by using different algorithms are reported in Appendix B. As can be seen from Table 3, when segmenting images with high levels of noise and INU artifact, the proposed method generally gives the best scores~~, except for CSF segmenting scores in terms of Hausdorff distance~~. Even though the scores for CSF are not the best, its values are comparable to the best one. Furthermore, Figs. 7–8 show the values of Dice coefficient (DICE) and Hausdorff distance (HD) in range of the obtained values for total segmented image using eight competing algorithms, respectively. It can be seen that our method performs better than the other ones for simulated brain MRI segmentation. Thus, the proposed algorithm provides more accurate and stable segmentation results than the counterparts when dealing with noise and intensity inhomogeneity problems.

5.5. Real MR brain images

We have also examined the ability of the proposed method when segmenting real MR images from Internet Brain Segmentation Repository (IBSR) database (the 20 normal T1-weighted MR brain images, which have a high level of intensity inhomogeneity, in the 4^{th}

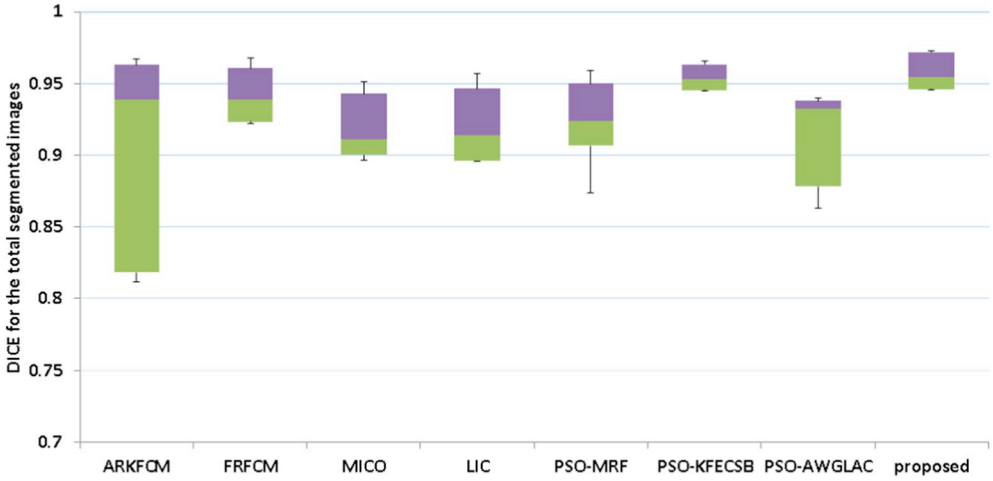

Fig. 7. Average values in terms of DICE coefficient on simulated MR brain images (slices 75, 80, 85, 95, 105, 115) using different algorithms.

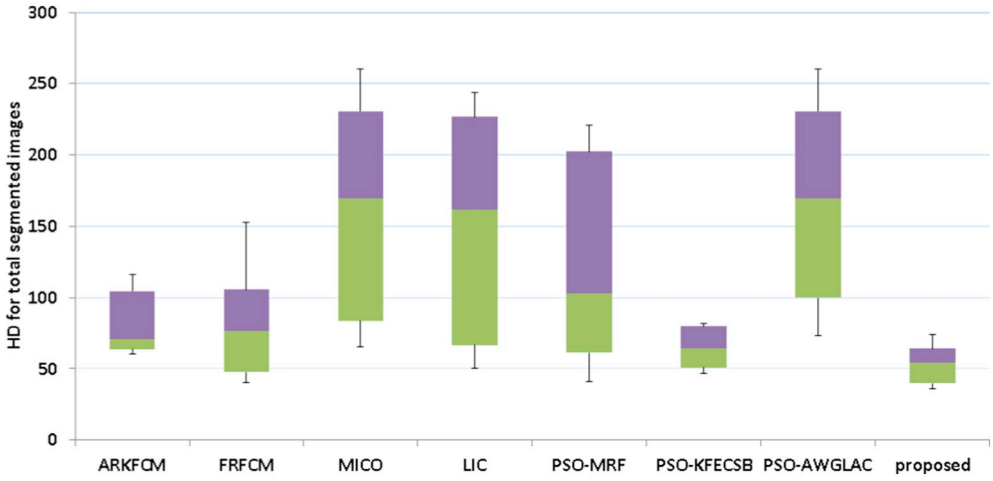

Fig. 8. Average values in terms of HD distance on simulated MR brain images (slices 75, 80, 85, 95, 105, 115) using different algorithms.

volume). Each image is segmented into three regions: cerebro spinal fluid (CSF), gray matter (GM) and white matter (WM). The background pixels are ignored in the computation. The rest of parameters is a set of the weighting coefficients ($\nu = 0.003 * 255^2$, $\rho = 0.4$, and $\zeta = 1.65$).

Fig. 10 shows the qualitative results of the segmentation by the competing algorithms. Taking a look at the results in this figure, it is clear that our proposed algorithm provides superior results, compared to others. Even though the PSO-KFECSB, PSO-AWGLAC, MICO, and LIC algorithms can provide a reasonable WM segmentation, they have difficulty to cope with smooth transient areas in the image. Fig. 13 shows qualitative results of the segmentation of five images (Z planes 24, 28, 32, 36, and 40) provided by the proposed algorithm. This figure shows that the proposed method has identified the tissues of the real MR images reasonably well.

Table 4 shows the average values of ~~the Dice coefficient and the Hausdorff distance~~five metrics when segmenting real MR brain images (Z planes 24, 28, 32, 34, 36, and 40) by different algorithms. These results show that the proposed method outperforms the ARKFCM, FRFCM, MICO, LIC, PSO-MRF, PSO-KFECSB, and PSO-AWGLAC algorithms. In addition, Figs. 11–12 show the values of Dice coefficient (DICE) and Hausdorff distance (HD), respectively, in range of the obtained values for total segmented image using eight competing algorithms. Again, the results presented here show the efficiency of the proposed approach and also demonstrate its superiority over the counterparts.

6. Discussion

6.1. Parameters setting

In this paper, there are two constant parameters (ρ, ζ) which control the effect of the GFE force and LFE force in the second objective

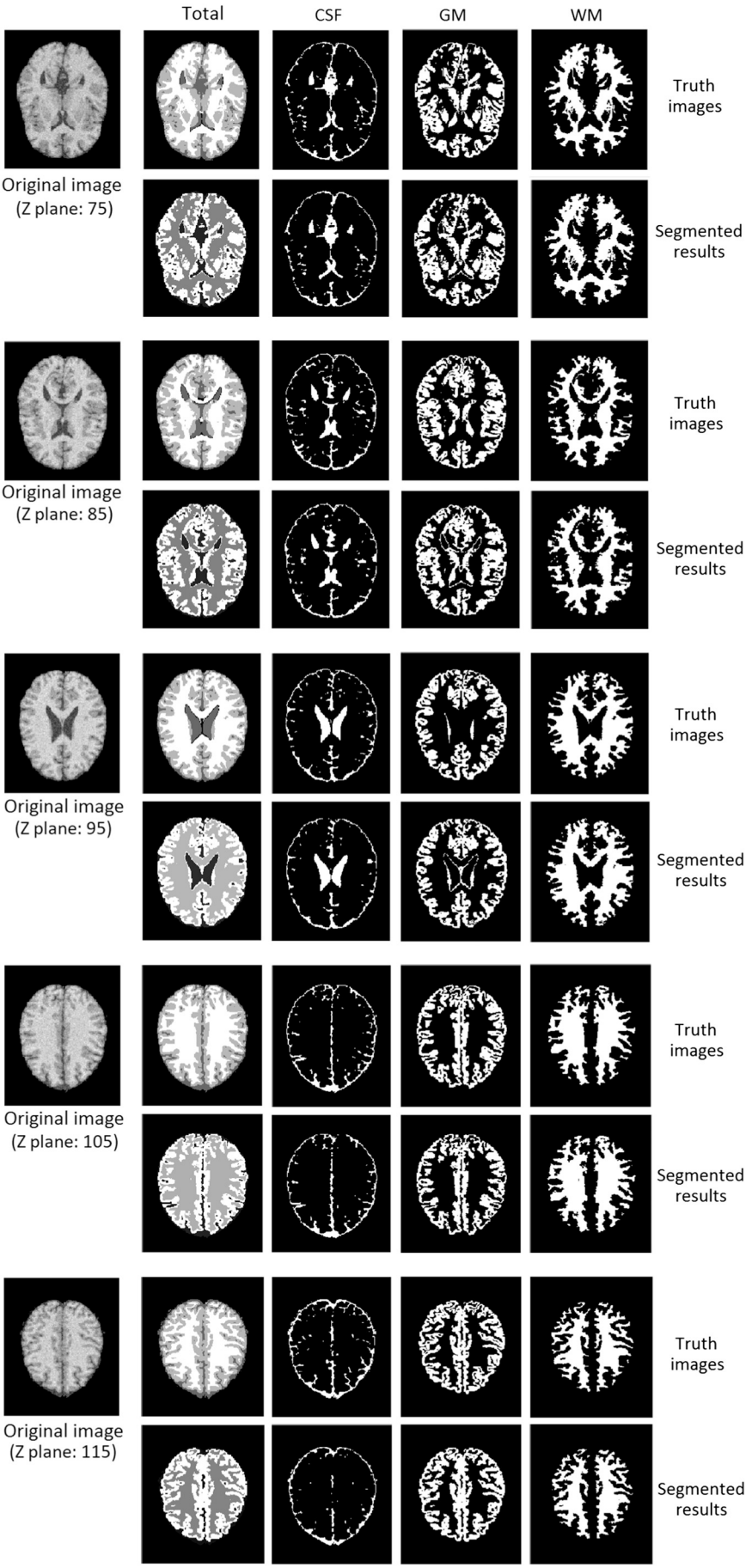

Fig. 9. Qualitative segmentation results of simulated MR brain images (slices 75, 85, 95, 105, 115) provided by the proposed algorithm versus the ground truth images.

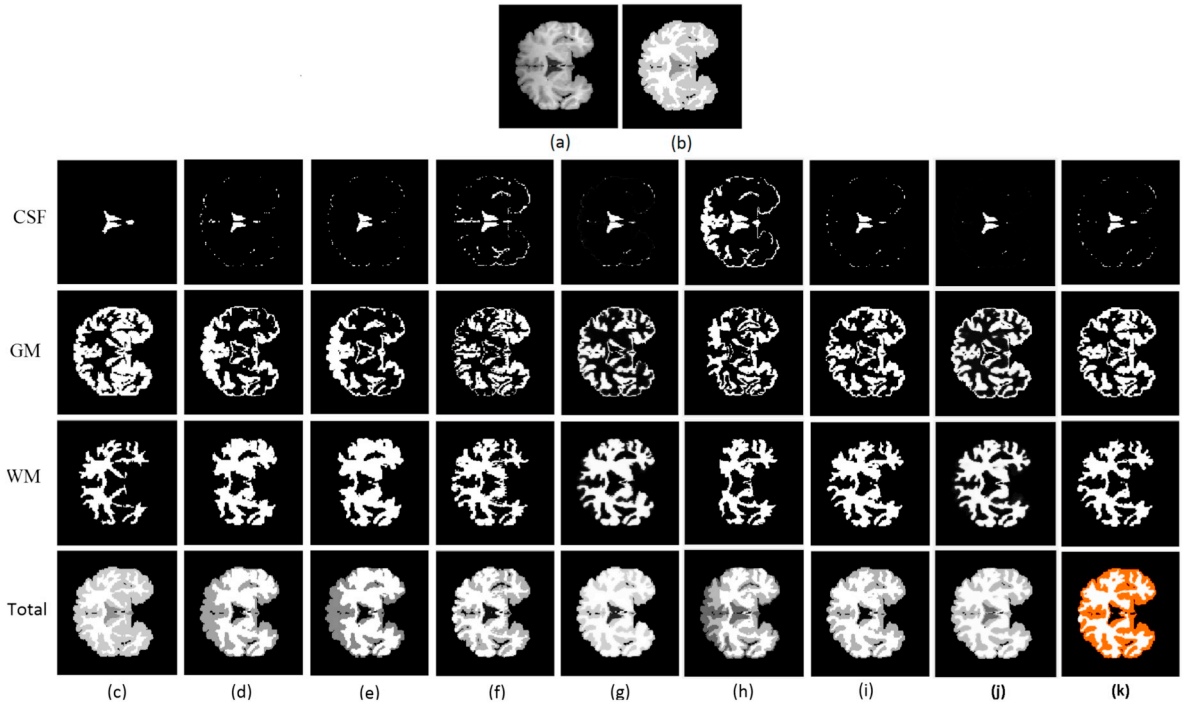

Fig. 10. Qualitative segmentation results of real MR brain image (Z plane 34 in the 4^{th} volume) provided by the competing algorithms: (a) original image; (b) original image after skull stripping; (c) ground truth images; (d) ARKFCM results; (e) FRFCM results; (f) MICO results; (g) LIC results; (h) PSO-MRF results; (i) PSO-KFECSB results; (j) PSO-AWGLAC results; (k) the proposed method results.

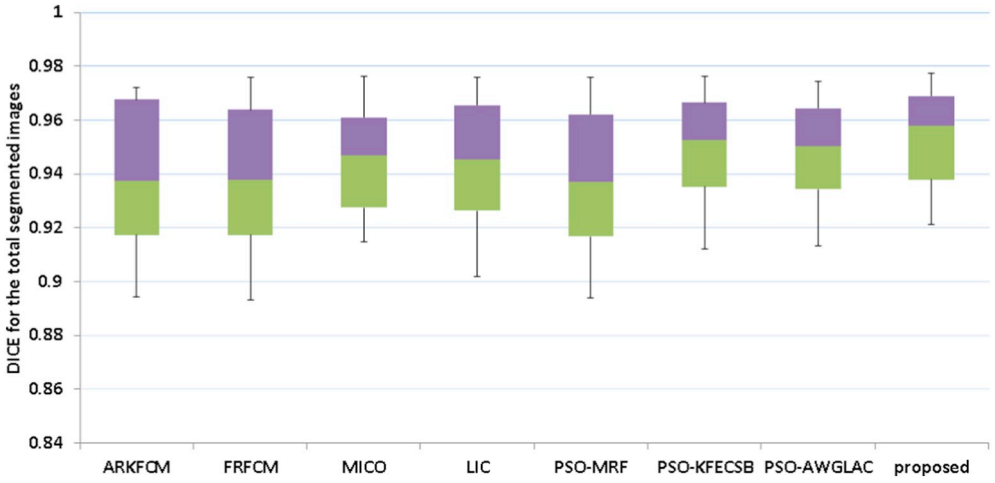

Fig. 11. Average values in terms of DICE coefficient on real MR brain images (slices 24, 28, 32, 34, 36, and 20) using different algorithms.

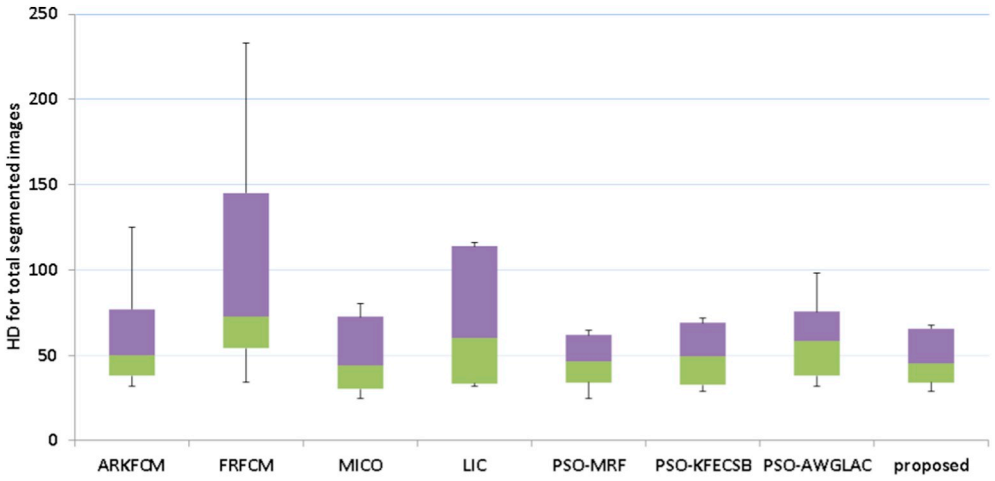

Fig. 12. Average values in terms of HD distance on real MR brain images (slices 24, 28, 32, 34, 36, and 20) using different algorithms.

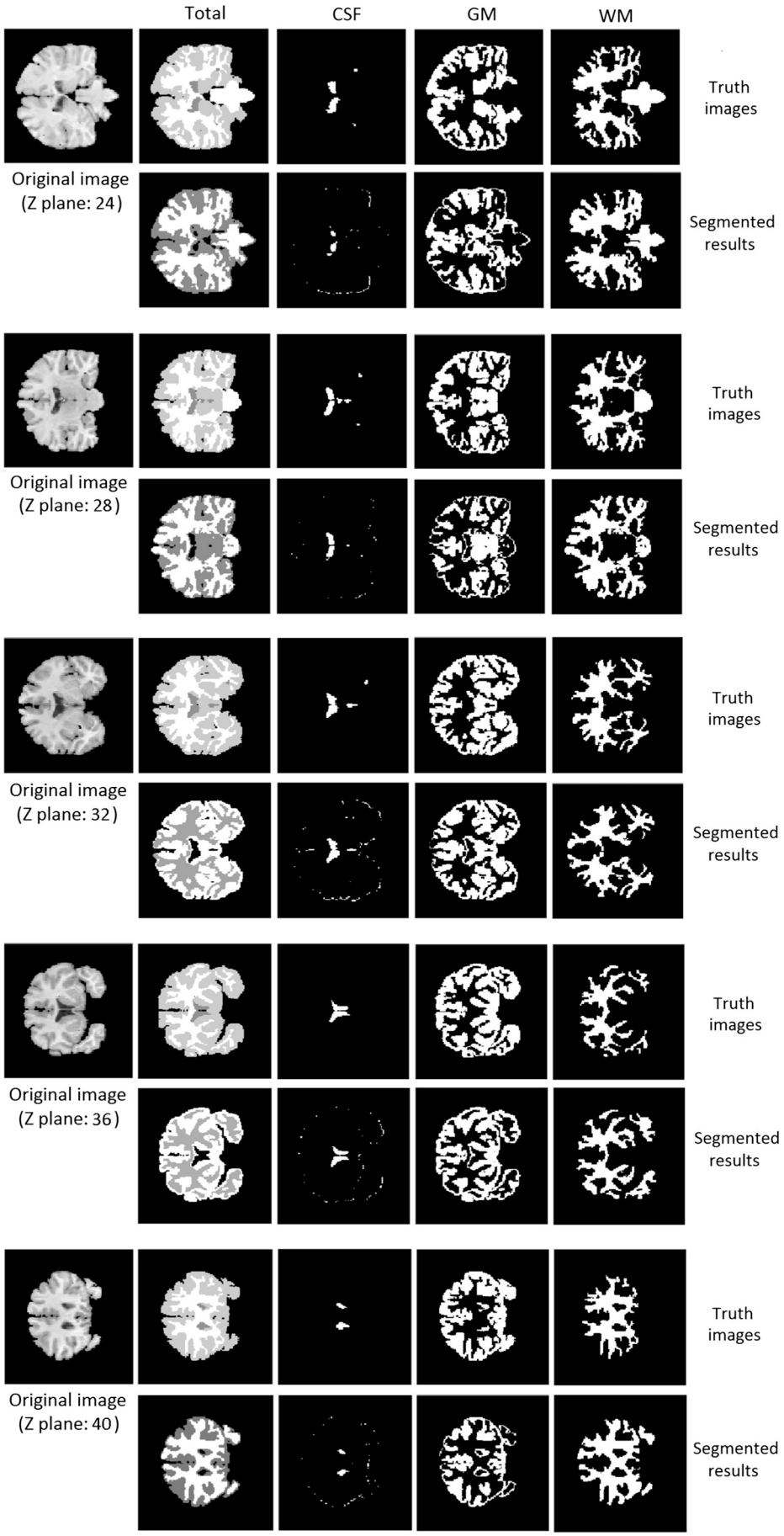

Fig. 13. Qualitative segmentation results of real MR brain images (Z planes 24, 28, 32, 36, 40 in the 4^{th} volume) by the proposed algorithm versus the ground truth images.

Table 4
Average values in terms of five criteria (DICE, HD, JAC, AC, SI) on real MR brain images using different algorithms.

Methods	Regions	Performance criteria				
		DICE	HD	JAC	AC	SI
ARKFCM	CSF	0.9574	1878.5000	0.9206	0.9221	0.9938
	GM	0.8496	166.6667	0.7425	0.7879	0.8059
	WM	0.8915	315.1667	0.8077	0.8437	0.9122
	Total	0.9387	59.6667	0.8888	0.9467	0.9510
FRFCM	CSF	0.9921	1877.8333	0.9843	0.9845	0.9904
	GM	0.8594	156.6667	0.7559	0.8008	0.8094
	WM	0.8646	175.0000	0.7649	0.8114	0.9228
	Total	0.9383	98.3333	0.8865	0.9446	0.9378
MICO	CSF	0.9715	1977.0000	0.9447	0.9457	**0.9974**[a]
	GM	0.8709	**143.1667**	0.7721	0.8160	0.8163
	WM	0.9014	129.3333	0.8217	0.8586	0.9429
	Total	0.9454	49.1667	0.8978	0.9508	0.9549
LIC	CSF	**0.9936**	**1745.5000**	**0.9878**	**0.9884**	0.9931
	GM	0.8760	147.3333	0.7805	0.8215	0.8159
	WM	0.8775	143.5000	0.7837	0.8300	0.9456
	Total	0.9442	69.3333	0.8953	0.9488	0.9403
PSO-MRF	CSF	0.9147	2011.6667	0.8431	0.8460	0.9970
	GM	0.8216	177.6667	0.6986	0.7450	0.7669
	WM	0.9026	423.0000	0.8254	0.8550	0.8991
	Total	0.9376	46.8333	0.8843	0.9449	0.9586
PSO-KFECSB	CSF	0.9932	1873.1667	0.9865	0.9867	0.9927
	GM	0.8902	146.0000	0.8027	0.8453	0.8428
	WM	0.8982	121.1667	0.8161	0.8557	0.9519
	Total	0.9499	50.3333	0.9054	0.9542	0.9504
PSO-AWGLAC	CSF	0.9931	2011.6667	0.9857	0.9862	0.9915
	GM	0.8853	147.8333	0.7961	0.8411	0.8397
	WM	0.8938	168.1667	0.8086	0.8476	0.9486
	Total	0.9485	59.1667	0.9025	0.9526	0.9495
Proposed	CSF	0.9931	1873.1667	0.9863	0.9865	0.9931
	GM	**0.8996**	145.1667	**0.8181**	**0.8609**	**0.8620**
	WM	**0.9103**	**119.1667**	**0.8362**	**0.8713**	**0.9530**
	Total	**0.9540**	**48.1667**	**0.9126**	**0.9580**	**0.9560**

[a] The bold numerical values indicate the best performance.

Table 5
Mean ± standard deviation of time cost of the proposed algorithm.

Dimension	Dataset	Number of images	Image size	Time/iteration (s)
2D	BrainWeb	10	181 × 217	4.76 ± 0.15
	IBSR	10	135 × 142	2.12 ± 0.06

function. These scale weights directly determine the accuracy of the proposed model, hence they indirectly define the quality of the proposed method. However, as pointed out in the Section 4.3.2, when the intensity inhomogeneity in the input image is severe, such as for real MR images in the IBSR database, the correctness of the proposed region-based active contour model relies on the LFE force. In such case, we should choose a higher value for (ζ); otherwise, the GFE force may cause the deformable curves falling into fake edges. For images with minor inhomogeneity and high level of noise, such as simulated MR images examined in Section 5.4, the influence of the GFE force in the model should be increased. In this situation, we can use a smaller value for (ζ) and a higher value for (ρ). In the experiment, we need to select appropriate values for (ρ, ζ) according to the degree of INU artifact and noise existing in input images.

6.2. Complexity analysis

The proposed method benefits both advantages of fuzzy entropy clustering and region-based active contour approaches to satisfy multiple requirements of image segmentation problem. In addition, using multiobjective particle swarm optimization algorithm to avoid the dependence on initial labelling is also taken into account. To analyze the complexity of the proposed algorithm, we calculated the running time when segmenting brain MR images. Both simulated and real brain MR image datasets are involved in experiments. Since the eventual computational cost will be the multiplication of cost for each iteration and the number of iterations for convergence, the average time cost of each iteration is recorded. The mean and standard deviation of the time cost of our algorithm (Intel Core i7 1.8 GHz CPU, 8 G RAM and Matlab 2014b) are listed in Table 5.

7. Conclusion

In this paper, we have proposed a new method, which is based on multi-objective optimization approach, for the segmentation of MR brain images. In the proposed method, an improved MOPSO algorithm, which takes advantages of the states-of-the-art developments in multi-objective clustering by using MOPSO method, is used to optimize two independent and complementary properties (compactness and separation) in segmented images. While the compactness is characterized by the first fitness function, called kernelized fuzzy entropy clustering with local spatial information and bias correction, the second property is represented by a novel region-based active contour model, called adaptive energy weight global and local fitting energy active contour model. The result of the optimization process is a set of Pareto-optimal solutions. By using the $\mathscr{L}_2$-metric method, the best trade-off solution is found and considered as the final result. In this way, the major drawbacks in fuzzy clustering and active contour methods (such as the sensitivity to noise, the INU artifact, the possibility to be trapped into the first local minimum they encounter when using the gradient descent search method), have been partially solved. Therefore, the algorithm can produce better segmentation results. To confirm the effectiveness of the proposed method, it has been examined on both simulated and real MR images, then compared to five recent segmentation methods in the literature. The experimental results show that our method can produce better segmentation results and is more robust against high levels of noise and INU artifact contained in input images. In particular, not only the visual segmentation is more accurate than others but also the quantitative results of segmentation show the better scores compared to the counterparts. However, in this method, the computational cost is high (using multiple convolution operations), and two parameters (ρ, ζ) are set based on the experiments. In the short term, the perspective for developing this work can be: (1) refining the two objective functions used for segmentation so as to reduce computational cost; (2) using an integrative approach combining the results of all solutions of the Pareto front instead of selecting the best estimated solution in this front.

Appendix A. Parameter setting for compared algorithms

The parameters for the compared algorithms are default values taken from their works as listed below.

Table A.1
Parameters setting used for the compared algorithms.

Algorithms	Parameters setting
ARKFCM	All the experiments are conducted with: number of clusters 4 (or 3 for real MR images), window size of 3×3 pixels, maximum number of iterations $t = 100$, median filter, and $\varepsilon = 0.001$.
FRFCM	All the experiments are conducted with: number of clusters 4 (or 3 for real MR images), window size of 3×3 pixels, square structuring element of size 3×3, maximum number of iterations $t = 100$, minimum amount of improvement $\eta = 0.001$, and exponent for the partition matrix $m = 2$.
MICO	All the experiments are conducted with: multiphase $N = 3$, 15 polynomials of the first four orders as the basis functions, maximum number of iterations $t = 15$, exponent for the partition matrix $q = 1$, and minimum amount of improvement $\varepsilon = 0.001$.
LIC	All the experiments are conducted with: multiphase $N = 3$, the convolution kernel is constructed as a 17×17 mask (scale parameter $\sigma = 4$), the time step $\Delta t = 0.1$, $\mu = 1$, weight of length term $\nu = 0.001 * 255^2$, $\varepsilon = 3$ for Heaviside function, number of inner iterations $N_i = 10$, and number of outer iterations $N_o = 100$.
PSO-MRF	All the experiments are conducted with: number of clusters 4, number of EM iterations $N_{em} = 3$, and number of MAP iterations $N_{map} = 3$.
PSO-KFECSB	All the experiments are conducted with: number of clusters 4 (or 3 for real MR images), the kernel parameter $\lambda = 1/9$, the population size $P = 100$, swarm size $N = 40$, constraints of the velocities $[-1,1]$, maximum number of iterations $k_{max} = 100$, termination criteria parameter $\epsilon = 0.0001$, the number of non-significant improvements $k_{stop} = 5$, and model parameters $n = 1/10$, $\eta = 2.5$.
PSO-AWGLAC	All the experiments are conducted with: number of clusters 4 (or 3 for real MR images), the population size $P = 100$, swarm size $N = 40$, constraints of the velocities $[-1,1]$, maximum number of iterations $k_{max} = 100$, the number of non-significant improvements $k_{stop} = 10$, the time step $\Delta t = 0.1$, $\mu = 1$, weight of length term $\nu = 0.003 * 255^2$, $\varepsilon = 3$, Gaussian parameter $\sigma = 4$, and scale parameters (ρ, ζ) are (1/1.9,1.9) (or (1/0.9,0.9) for real MR images).

Appendix B. Average values in terms of criteria on simulated MR brain images using different algorithms

The experimental results for several T1-weighted slices downloaded from the BrainWeb (with 9% noise and 40% INU artifact).

Table B.1
Average values of criteria on slice 75 using different algorithms.

Slice	Methods	Regions	Performance criteria				
			DICE	HD	JAC	AC	SI
75	ARKFCM	CSF	0.9851	130	0.9707	0.9742	0.9864
		GM	0.9128	73	0.8396	0.8868	0.9162
		WM	0.9321	88	0.8728	0.9114	0.9289
		Total	0.9269	68	0.8639	0.951	0.9287
75	FRFCM	CSF	0.9777	389	0.9564	0.9611	0.9742
		GM	0.9089	90	0.833	0.881	0.9063
		WM	0.9316	90	0.8721	0.9117	0.9371
		Total	0.9218	90	0.855	0.9473	0.9201
75	MICO	CSF	0.9819	212	0.9645	0.9687	0.9869
		GM	0.8756	170	0.7788	0.8362	0.8661
		WM	0.8959	170	0.8114	0.8659	0.9041
		Total	0.9015	170	0.8208	0.9341	0.9053
75	LIC	CSF	0.9835	160	0.9676	0.9712	0.9774
		GM	0.8695	170	0.7691	0.8255	0.8481
		WM	0.8827	170	0.79	0.8522	0.911
		Total	0.8961	170	0.8118	0.9298	0.8923
75	PSO-MRF	CSF	0.9776	200	0.9562	0.9616	0.9922
		GM	0.896	117	0.8116	0.8631	0.8871
		WM	0.9226	117	0.8563	0.8994	0.9225
		Total	0.9176	117	0.8478	0.9451	0.9257
75	PSO-KFECSB	CSF	0.9859	167	0.9723	0.9751	0.9811
		GM	0.9359	65	0.8796	0.9162	0.9328
		WM	0.9543	81	0.9127	0.941	0.9588
		Total	0.945	67	0.8957	0.9631	0.9462
75	PSO-AWGLAC	CSF	0.9854	373	0.9712	0.9744	0.9768
		GM	0.9202	170	0.8522	0.897	0.9291
		WM	0.9417	170	0.8899	0.9242	0.9408
		Total	0.9344	170	0.8769	0.9558	0.9323
75	Proposed	CSF	0.9859	153	0.9723	0.9754	0.9814
		GM	0.9365	65	0.8805	0.9171	0.9347
		WM	0.9551	80	0.914	0.9421	0.9623
		Total	0.9459	61	0.8974	0.9636	0.9451

Table B.2
Average values of criteria on slice 80 using different algorithms.

Slice	Methods	Regions	Performance criteria				
			DICE	HD	JAC	AC	SI
80	ARKFCM	CSF	0.8024	226	0.6701	0.6825	0.855
		GM	0.7865	72	0.6481	0.7058	0.7252
		WM	0.9341	145	0.8763	0.9061	0.9051
		Total	0.812	60	0.6835	0.8669	0.7748
80	FRFCM	CSF	0.9719	580	0.9454	0.9516	0.9628
		GM	0.9075	153	0.8307	0.8828	0.9035
		WM	0.9425	225	0.8913	0.9217	0.9548
		Total	0.9238	153	0.8584	0.9485	0.9208
80	MICO	CSF	0.9761	140	0.9534	0.9594	0.9793
		GM	0.8622	85	0.7578	0.8221	0.8429
		WM	0.8955	208	0.8108	0.8593	0.9173
		Total	0.8967	65	0.8128	0.9308	0.902
80	LIC	CSF	0.9789	89	0.9586	0.9636	0.9684
		GM	0.8608	72	0.7556	0.8194	0.8372
		WM	0.8889	208	0.8	0.8528	0.9267
		Total	0.8956	50	0.811	0.9296	0.8947
80	PSO-MRF	CSF	0.974	74	0.9493	0.9563	0.9888
		GM	0.8976	61	0.8143	0.8685	0.8811
		WM	0.9346	89	0.8773	0.9107	0.9434
		Total	0.922	41	0.8552	0.9479	0.9314
80	PSO-KFECSB	CSF	0.9801	145	0.9618	0.9654	0.9749
		GM	0.9334	61	0.8752	0.916	0.9326
		WM	0.9607	81	0.9244	0.9461	0.9658
		Total	0.9456	52	0.8968	0.9633	0.946
80	PSO-AWGLAC	CSF	0.9209	305	0.8535	0.8536	0.8536
		GM	0.9186	85	0.8495	0.8979	0.9231
		WM	0.9517	218	0.9078	0.9339	0.96
		Total	0.8631	73	0.7592	0.8995	0.7978
80	Proposed	CSF	0.9806	136	0.9619	0.9668	0.9758
		GM	0.9338	61	0.8759	0.9169	0.9371
		WM	0.963	81	0.9287	0.9491	0.9649
		Total	0.9462	58	0.8979	0.9637	0.9453

Table B.3
Average values of criteria on slice 85 using different algorithms.

Slice	Methods	Regions	Performance criteria				
			DICE	HD	JAC	AC	SI
85	ARKFCM	CSF	0.8091	170	0.6794	0.6892	0.8629
		GM	0.7909	125	0.6541	0.7037	0.7368
		WM	0.9259	106	0.862	0.8969	0.8891
		Total	0.8203	73	0.6954	0.8703	0.7841
85	FRFCM	CSF	0.9762	442	0.9536	0.9588	0.9732
		GM	0.9197	106	0.8513	0.895	0.9238
		WM	0.947	130	0.8994	0.9294	0.9473
		Total	0.9306	85	0.8703	0.9522	0.9311
85	MICO	CSF	0.9769	169	0.9549	0.9603	0.9729
		GM	0.8782	125	0.7829	0.8376	0.8647
		WM	0.9061	98	0.8283	0.8765	0.9197
		Total	0.9062	90	0.8285	0.9358	0.9122
85	LIC	CSF	0.9801	328	0.9609	0.9653	0.9729
		GM	0.8748	125	0.7774	0.8314	0.8537
		WM	0.8965	100	0.8125	0.8665	0.9283
		Total	0.9035	72	0.824	0.9334	0.9022
85	PSO-MRF	CSF	0.9739	226	0.9492	0.9557	0.9905
		GM	0.9039	113	0.8246	0.8727	0.8965
		WM	0.9386	82	0.8843	0.9179	0.9369
		Total	0.9256	68	0.8615	0.9493	0.936
85	PSO-KFECSB	CSF	0.9733	328	0.9621	0.9608	0.9719
		GM	0.9362	125	0.88	0.9162	0.9356
		WM	0.9613	91	0.9255	0.9486	0.9666
		Total	0.946	61	0.8975	0.9629	0.9487
85	PSO-AWGLAC	CSF	0.9802	260	0.9613	0.9653	0.9663
		GM	0.9235	125	0.858	0.9008	0.9347
		WM	0.9557	173	0.9153	0.9412	0.9596
		Total	0.9399	109	0.8867	0.9585	0.9375

(*continued on next page*)

Table B.3 (*continued*)

Slice	Methods	Regions	Performance criteria				
			DICE	HD	JAC	AC	SI
85	Proposed	CSF	0.9833	333	0.9671	0.9709	0.9788
		GM	0.9387	125	0.8845	0.9201	0.9446
		WM	0.9646	89	0.9316	0.9528	0.9656
		Total	0.9479	50	0.9009	0.9641	0.9489

Table B.4
Average values of criteria on slice 95 using different algorithms.

Slice	Methods	Regions	Performance criteria				
			DICE	HD	JAC	AC	SI
95	ARKFCM	CSF	0.9869	338	0.9741	0.9773	0.9865
		GM	0.9413	272	0.8892	0.9165	0.9551
		WM	0.9569	74	0.9175	0.9447	0.9487
		Total	0.9514	65	0.9073	0.965	0.9575
95	FRFCM	CSF	0.9809	338	0.9626	0.9669	0.9765
		GM	0.9392	281	0.8854	0.9132	0.9499
		WM	0.9556	74	0.9151	0.9433	0.9522
		Total	0.9472	50	0.8997	0.9618	0.9498
95	MICO	CSF	0.9837	181	0.9681	0.972	0.9857
		GM	0.8876	272	0.7979	0.8389	0.8945
		WM	0.8968	221	0.813	0.8681	0.8935
		Total	0.9161	221	0.8452	0.9396	0.9226
95	LIC	CSF	0.9853	340	0.9711	0.9745	0.9774
		GM	0.9024	272	0.8222	0.8564	0.8856
		WM	0.9066	221	0.8292	0.8842	0.9319
		Total	0.925	221	0.8605	0.9454	0.92
95	PSO-MRF	CSF	0.9836	130	0.9679	0.972	0.992
		GM	0.9323	272	0.8732	0.9027	0.937
		WM	0.9491	221	0.9032	0.9348	0.9429
		Total	0.9468	221	0.8989	0.9618	0.9558
95	PSO-KFECSB	CSF	0.9774	353	0.9645	0.9676	0.9703
		GM	0.9523	272	0.9102	0.9322	0.9569
		WM	0.9693	67	0.9405	0.9611	0.9745
		Total	0.9606	47	0.924	0.9712	0.9624
95	PSO-AWGLAC	CSF	0.9273	421	0.8646	0.8646	0.8646
		GM	0.9402	272	0.8872	0.9142	0.9463
		WM	0.9598	221	0.9228	0.9493	0.9684
		Total	0.8829	221	0.7903	0.9085	0.8229
95	Proposed	CSF	0.9875	353	0.9755	0.9784	0.9808
		GM	0.9532	272	0.9106	0.9328	0.9582
		WM	0.9695	64	0.9408	0.9614	0.9748
		Total	0.961	41	0.9249	0.9718	0.9629

Table B.5
Average values of criteria on slice 105 using different algorithms.

Slice	Methods	Regions	Performance criteria				
			DICE	HD	JAC	AC	SI
105	ARKFCM	CSF	0.9751	129	0.9606	0.9632	0.9689
		GM	0.9434	101	0.8928	0.9202	0.9498
		WM	0.9571	121	0.9177	0.9428	0.9466
		Total	0.964	101	0.9305	0.972	0.9649
105	FRFCM	CSF	0.9785	421	0.9579	0.9613	0.9826
		GM	0.9377	40	0.8827	0.912	0.9426
		WM	0.9562	477	0.9161	0.9416	0.9449
		Total	0.9583	40	0.92	0.9675	0.9572
105	MICO	CSF	0.9786	200	0.9581	0.9617	0.9875
		GM	0.8978	260	0.8146	0.853	0.8858
		WM	0.9133	260	0.8405	0.8863	0.9177
		Total	0.9398	260	0.8864	0.9532	0.9416
105	LIC	CSF	0.9839	109	0.9683	0.9707	0.977
		GM	0.9065	244	0.8291	0.8637	0.8824
		WM	0.9129	244	0.8397	0.8886	0.9412
		Total	0.943	244	0.8922	0.9553	0.9346

(*continued on next page*)

Table B.5 (*continued*)

Slice	Methods	Regions	Performance criteria				
			DICE	HD	JAC	AC	SI
105	PSO-MRF	CSF	0.977	169	0.9551	0.9592	0.9954
		GM	0.9278	196	0.8654	0.8971	0.9227
		WM	0.951	196	0.9067	0.9348	0.9408
		Total	0.9591	196	0.9214	0.9684	0.9655
105	PSO-KFECSB	CSF	0.984	130	0.9644	0.9648	0.9713
		GM	0.9529	82	0.9103	0.9321	0.9464
		WM	0.9693	120	0.9405	0.9599	0.9764
		Total	0.9625	82	0.9456	0.9686	0.9609
105	PSO-AWGLAC	CSF	0.9493	585	0.9035	0.9035	0.9035
		GM	0.923	260	0.857	0.8905	0.9207
		WM	0.9511	260	0.9068	0.937	0.9732
		Total	0.9305	260	0.87	0.9436	0.8931
105	Proposed	CSF	0.9842	128	0.9689	0.9711	0.9715
		GM	0.9531	36	0.9104	0.9334	0.9531
		WM	0.9694	113	0.9407	0.9601	0.9799
		Total	0.9725	36	0.9465	0.9785	0.9662

Table B.6
Average values of criteria on slice 115 using different algorithms.

Slice	Methods	Regions	Performance criteria				
			DICE	HD	JAC	AC	SI
115	ARKFCM	CSF	0.9865	221	0.9735	0.9758	0.9847
		GM	0.9301	116	0.8717	0.9003	0.9503
		WM	0.9645	116	0.9315	0.9487	0.961
		Total	0.9624	116	0.9433	0.9682	0.9494
115	FRFCM	CSF	0.9804	709	0.9616	0.9646	0.9752
		GM	0.9314	78	0.8704	0.9003	0.9472
		WM	0.9629	265	0.9285	0.9464	0.9607
		Total	0.9675	68	0.937	0.9719	0.962
115	MICO	CSF	0.9779	205	0.9568	0.9605	0.983
		GM	0.8952	169	0.8103	0.8475	0.8797
		WM	0.9167	169	0.8462	0.8814	0.9284
		Total	0.9516	169	0.9077	0.9585	0.9525
115	LIC	CSF	0.9849	145	0.9703	0.9726	0.9756
		GM	0.9107	153	0.8361	0.8691	0.8879
		WM	0.923	153	0.8571	0.8926	0.955
		Total	0.9571	153	0.9178	0.963	0.9525
115	PSO-MRF	CSF	0.9084	485	0.8322	0.8367	0.9208
		GM	0.94	116	0.8869	0.9134	0.9307
		WM	0.9591	116	0.9214	0.941	0.9588
		Total	0.8738	89	0.7759	0.89	0.8929
115	PSO-KFECSB	CSF	0.9775	221	0.9553	0.9475	0.9453
		GM	0.9377	79	0.8989	0.9091	0.9502
		WM	0.9695	29	0.9409	0.9564	0.9742
		Total	0.9658	79	0.9428	0.9692	0.9622
115	PSO-AWGLAC	CSF	0.964	337	0.9305	0.9329	0.9317
		GM	0.8415	169	0.7264	0.7567	0.7871
		WM	0.8562	185	0.7485	0.8096	0.9405
		Total	0.9372	169	0.8819	0.9446	0.912
115	Proposed	CSF	0.9698	304	0.9414	0.9441	0.9428
		GM	0.9317	74	0.8721	0.9044	0.9522
		WM	0.9707	29	0.943	0.9579	0.9751
		Total	0.9714	74	0.9444	0.9753	0.9623

Appendix C. Average values in terms of criteria on real MR brain images using different algorithms

The experimental results for several T1-weighted slices (in 20 normal MR brain dataset) provided by the Center for Morphometric Analysis at Massachusetts General Hospital, which are available at http://www.nitrc.org/projects/ibsr/.

Table C.1
Average values of criteria on slice 24 using different algorithms.

Slice	Methods	Regions	Performance criteria				
			DICE	HD	JAC	AC	SI
24	ARKFCM	CSF	0.9874	1480	0.9752	0.9753	0.9825
		GM	0.8028	338	0.6706	0.7274	0.7615
		WM	0.799	260	0.6653	0.7428	0.8447
		Total	0.8941	125	0.8085	0.9131	0.8857
24	FRFCM	CSF	0.9864	1480	0.9732	0.9733	0.9805
		GM	0.8	338	0.6667	0.7204	0.7512
		WM	0.792	233	0.6557	0.7362	0.8456
		Total	0.8931	233	0.8068	0.9119	0.8812
24	MICO	CSF	0.9696	2098	0.941	0.9421	0.9972
		GM	0.8518	313	0.7419	0.792	0.7971
		WM	0.8674	137	0.7658	0.8281	0.9041
		Total	0.9149	52	0.8432	0.9312	0.9201
24	LIC	CSF	0.9887	1480	0.9777	0.9779	0.9837
		GM	0.8265	338	0.7044	0.7473	0.7496
		WM	0.8079	137	0.6777	0.7622	0.8875
		Total	0.9019	113	0.8213	0.9179	0.8765
24	PSO-MRF	CSF	0.8903	2098	0.8023	0.8062	0.9957
		GM	0.7688	373	0.6244	0.6773	0.7231
		WM	0.8357	661	0.7179	0.7708	0.8088
		Total	0.8939	65	0.8082	0.9165	0.9247
24	PSO-KFECSB	CSF	0.9884	1480	0.9771	0.9773	0.9841
		GM	0.8494	338	0.7383	0.7907	0.8015
		WM	0.8485	90	0.7368	0.8068	0.9008
		Total	0.912	58	0.8383	0.9277	0.9023
24	PSO-AWGLAC	CSF	0.985	2098	0.9702	0.9703	0.9838
		GM	0.8497	338	0.7495	0.8057	0.8203
		WM	0.8593	157	0.7546	0.8116	0.9002
		Total	0.9133	98	0.8375	0.9274	0.9097
24	Proposed	CSF	0.9887	1480	0.9777	0.9779	0.9849
		GM	0.8658	338	0.7633	0.8197	0.8432
		WM	0.8752	90	0.7781	0.8364	0.9017
		Total	0.9211	50	0.8538	0.9357	0.9182

Table C.2
Average values of criteria on slice 28 using different algorithms.

Slice	Methods	Regions	Performance criteria				
			DICE	HD	JAC	AC	SI
28	ARKFCM	CSF	0.917	1557	0.8468	0.8497	0.9941
		GM	0.8055	313	0.6744	0.7197	0.7573
		WM	0.8675	626	0.7661	0.8103	0.8606
		Total	0.925	50	0.8605	0.9351	0.9452
28	FRFCM	CSF	0.9911	1557	0.9825	0.9827	0.9871
		GM	0.8392	338	0.7229	0.7685	0.7899
		WM	0.8335	292	0.7146	0.7774	0.8889
		Total	0.9254	116	0.8612	0.9335	0.9178
28	MICO	CSF	0.9558	1557	0.9153	0.917	0.9948
		GM	0.8416	338	0.7265	0.7728	0.7947
		WM	0.8804	104	0.7865	0.8339	0.9007
		Total	0.9315	80	0.8718	0.9401	0.9425
28	LIC	CSF	0.9945	1105	0.9892	0.9894	0.9905
		GM	0.8679	338	0.7667	0.8069	0.8059
		WM	0.8588	116	0.7526	0.8133	0.9276
		Total	0.9344	116	0.8768	0.9412	0.9228
28	PSO-MRF	CSF	0.9106	1557	0.8359	0.8392	0.9947
		GM	0.8006	313	0.6675	0.7136	0.755
		WM	0.8668	776	0.765	0.8074	0.8515
		Total	0.9245	53	0.8597	0.9348	0.9461
28	PSO-KFECSB	CSF	0.9932	1525	0.9866	0.9868	0.9899
		GM	0.8871	338	0.7972	0.8393	0.8429
		WM	0.8878	82	0.7983	0.8487	0.9376
		Total	0.9428	68	0.8918	0.9491	0.9376
28	PSO-AWGLAC	CSF	0.9927	1557	0.9845	0.9857	0.9879
		GM	0.8847	338	0.7914	0.8401	0.8431
		WM	0.8902	106	0.8013	0.8511	0.9316
		Total	0.9411	68	0.8911	0.9484	0.9386

(*continued on next page*)

Table C.2 (*continued*)

Slice	Methods	Regions	Performance criteria				
			DICE	HD	JAC	AC	SI
28	Proposed	CSF	0.9932	1525	0.9866	0.9868	0.9899
		GM	0.8887	338	0.7997	0.842	0.8469
		WM	0.8902	82	0.8021	0.8515	0.9374
		Total	0.9435	68	0.8931	0.9498	0.939

Table C.3
Average values of criteria on slice 32 using different algorithms.

Slice	Methods	Regions	Performance criteria				
			DICE	HD	JAC	AC	SI
32	ARKFCM	CSF	0.927	2385	0.864	0.8668	0.9966
		GM	0.8146	149	0.6872	0.7399	0.7532
		WM	0.8923	410	0.8056	0.8395	0.9099
		Total	0.9304	61	0.8698	0.9382	0.953
32	FRFCM	CSF	0.9926	2329	0.9854	0.9857	0.9914
		GM	0.839	85	0.7227	0.7746	0.777
		WM	0.8463	125	0.7336	0.7841	0.921
		Total	0.9307	85	0.8704	0.937	0.9305
32	MICO	CSF	0.9738	2385	0.9489	0.9499	0.997
		GM	0.864	70	0.7605	0.8125	0.8111
		WM	0.8987	80	0.8161	0.853	0.9423
		Total	0.9403	70	0.8874	0.9465	0.952
32	LIC	CSF	0.9942	2340	0.9885	0.9887	0.9946
		GM	0.8716	80	0.7724	0.8219	0.8141
		WM	0.8805	80	0.7865	0.8305	0.9482
		Total	0.9409	80	0.8883	0.9464	0.943
32	PSO-MRF	CSF	0.9192	2385	0.8505	0.8536	0.9969
		GM	0.8099	157	0.6806	0.7334	0.7489
		WM	0.8933	449	0.8073	0.8399	0.9038
		Total	0.9301	61	0.8693	0.938	0.954
32	PSO-KFECSB	CSF	0.9928	2385	0.9858	0.9861	0.9935
		GM	0.8863	72	0.7958	0.8446	0.8386
		WM	0.8994	72	0.8172	0.8556	0.9552
		Total	0.9468	72	0.899	0.9519	0.9507
32	PSO-AWGLAC	CSF	0.9961	2385	0.9923	0.9925	0.9942
		GM	0.8799	72	0.7856	0.8354	0.8303
		WM	0.889	157	0.8001	0.8414	0.9491
		Total	0.9441	68	0.8942	0.9494	0.9467
32	Proposed	CSF	0.9921	2385	0.9844	0.9846	0.9945
		GM	0.8926	65	0.8061	0.8545	0.8506
		WM	0.9082	65	0.8319	0.8672	0.9558
		Total	0.9497	65	0.9042	0.9545	0.9548

Table C.4
Average values of criteria on slice 34 using different algorithms.

Slice	Methods	Regions	Performance criteria				
			DICE	HD	JAC	AC	SI
34	ARKFCM	CSF	0.9238	2313	0.8585	0.8617	0.9976
		GM	0.8274	97	0.7056	0.7553	0.7682
		WM	0.9139	289	0.8415	0.8661	0.9234
		Total	0.944	40	0.894	0.9476	0.9651
34	FRFCM	CSF	0.9935	2313	0.9871	0.9873	0.9932
		GM	0.856	61	0.7482	0.7965	0.797
		WM	0.8675	85	0.766	0.8064	0.9387
		Total	0.9445	61	0.8949	0.9471	0.9474
34	MICO	CSF	0.9809	2234	0.9626	0.9634	0.9975
		GM	0.8843	40	0.7927	0.8376	0.8279
		WM	0.912	90	0.8382	0.8689	0.9654
		Total	0.9535	32	0.9111	0.9559	0.963
34	LIC	CSF	0.995	2234	0.9901	0.9903	0.9958
		GM	0.8771	41	0.7811	0.8256	0.8139
		WM	0.8858	130	0.795	0.8335	0.9611
		Total	0.95	41	0.9048	0.9523	0.9528

(*continued on next page*)

Table C.4 (*continued*)

Slice	Methods	Regions	Performance criteria				
			DICE	HD	JAC	AC	SI
34	PSO-MRF	CSF	0.9246	2313	0.8598	0.863	0.9976
		GM	0.8267	97	0.7046	0.7546	0.7684
		WM	0.9126	289	0.8392	0.8639	0.9216
		Total	0.9437	40	0.8934	0.9473	0.9647
34	PSO-KFECSB	CSF	0.9939	2313	0.9879	0.9881	0.9949
		GM	0.9009	41	0.8197	0.8629	0.854
		WM	0.9147	85	0.8428	0.8731	0.9696
		Total	0.9584	41	0.9201	0.9604	0.9636
34	PSO-AWGLAC	CSF	0.9959	2313	0.9918	0.9919	0.9932
		GM	0.8961	49	0.8119	0.856	0.848
		WM	0.9073	145	0.8303	0.8628	0.967
		Total	0.9566	49	0.9169	0.9587	0.9604
34	Proposed	CSF	0.9936	2313	0.9873	0.9875	0.9951
		GM	0.9208	41	0.8533	0.8925	0.8883
		WM	0.9364	85	0.8804	0.9037	0.9733
		Total	0.9663	41	0.9348	0.9679	0.9717

Table C.5
Average values of criteria on slice 36 using different algorithms.

Slice	Methods	Regions	Performance criteria				
			DICE	HD	JAC	AC	SI
36	ARKFCM	CSF	0.9943	2176	0.9887	0.9888	0.9969
		GM	0.9063	50	0.8286	0.8724	0.8768
		WM	0.9256	72	0.8616	0.8821	0.9584
		Total	0.9662	50	0.9346	0.9659	0.9728
36	FRFCM	CSF	0.9942	2228	0.9886	0.9887	0.9962
		GM	0.8864	73	0.7961	0.8405	0.8337
		WM	0.9025	81	0.8224	0.8499	0.9651
		Total	0.9599	61	0.9229	0.9595	0.967
36	MICO	CSF	0.9851	2228	0.9707	0.9713	0.9985
		GM	0.8721	45	0.7732	0.8163	0.8045
		WM	0.8949	100	0.8099	0.8397	0.967
		Total	0.956	25	0.9157	0.9556	0.965
36	LIC	CSF	0.9948	2176	0.9897	0.9899	0.9965
		GM	0.8949	34	0.8098	0.8523	0.8412
		WM	0.9095	100	0.8341	0.8608	0.9735
		Total	0.9621	32	0.927	0.9617	0.9692
36	PSO-MRF	CSF	0.9231	2228	0.8573	0.8598	0.9982
		GM	0.8461	41	0.7333	0.7821	0.7901
		WM	0.9422	178	0.8907	0.9055	0.9446
		Total	0.9574	37	0.9182	0.9575	0.9724
36	PSO-KFECSB	CSF	0.9947	2176	0.9895	0.9897	0.9972
		GM	0.8995	34	0.8174	0.859	0.847
		WM	0.9143	100	0.8422	0.8679	0.9759
		Total	0.9634	34	0.9295	0.9631	0.9708
36	PSO-AWGLAC	CSF	0.9941	2228	0.9843	0.9844	0.9957
		GM	0.8914	37	0.804	0.8471	0.8368
		WM	0.9033	130	0.8237	0.8518	0.9711
		Total	0.9612	32	0.9253	0.9608	0.9672
36	Proposed	CSF	0.9949	2176	0.9898	0.99	0.9972
		GM	0.9068	36	0.8295	0.8733	0.8598
		WM	0.922	100	0.8554	0.8789	0.9767
		Total	0.9657	36	0.9338	0.9654	0.9732

Table C.6
Average values of criteria on slice 40 using different algorithms.

Slice	Methods	Regions	Performance criteria				
			DICE	HD	JAC	AC	SI
40	ARKFCM	CSF	0.9951	1360	0.9904	0.9904	0.995
		GM	0.941	53	0.8886	0.9128	0.9183
		WM	0.9508	234	0.9063	0.9216	0.9759
		Total	0.9723	32	0.9653	0.98	0.9841

(*continued on next page*)

Table C.6 (*continued*)

Slice	Methods	Regions	Performance criteria				
			DICE	HD	JAC	AC	SI
40	FRFCM	CSF	0.9945	1360	0.9891	0.9892	0.9939
		GM	0.9356	45	0.879	0.9042	0.9077
		WM	0.9458	234	0.8972	0.9141	0.9772
		Total	0.9759	34	0.9625	0.9784	0.9827
40	MICO	CSF	0.9636	1360	0.9298	0.9305	0.9996
		GM	0.9116	53	0.8376	0.865	0.8624
		WM	0.9547	265	0.9134	0.9277	0.9776
		Total	0.9762	36	0.9573	0.9755	0.9865
40	LIC	CSF	0.9942	1138	0.9914	0.9944	0.9975
		GM	0.918	53	0.8484	0.875	0.8708
		WM	0.9226	298	0.8563	0.8799	0.9756
		Total	0.9761	34	0.9535	0.973	0.9772
40	PSO-MRF	CSF	0.9206	1489	0.8529	0.8542	0.9991
		GM	0.8772	85	0.7813	0.8088	0.8161
		WM	0.9648	185	0.932	0.9423	0.9641
		Total	0.9761	25	0.9572	0.9755	0.9899
40	PSO-KFECSB	CSF	0.9959	1360	0.9919	0.9919	0.9965
		GM	0.9177	53	0.848	0.875	0.8729
		WM	0.9242	298	0.8591	0.882	0.9723
		Total	0.9762	29	0.9536	0.9731	0.9776
40	PSO-AWGLAC	CSF	0.995	1489	0.9911	0.9921	0.9944
		GM	0.9097	53	0.8344	0.862	0.8598
		WM	0.9138	314	0.8414	0.867	0.9728
		Total	0.9744	40	0.9502	0.9711	0.9743
40	Proposed	CSF	0.996	1360	0.992	0.9921	0.9971
		GM	0.9226	53	0.8564	0.8833	0.8832
		WM	0.93	293	0.8692	0.8903	0.973
		Total	0.9774	29	0.9558	0.9745	0.9793

References

[1] Gonzalez RC, Woods RE. Digital image processing. Prentice Hall; 2012.
[2] Simmons A, Tofts PS, Barker GJ, Arridge SR. Sources of intensity nonuniformity in spin echo images at 1.5 T. Magn Reson Med 1994;32(1):121–8.
[3] Clarke L, Velthuizen R, Camacho M, Heine J, Vaidyanathan M, Hall L, et al. MRI segmentation: methods and applications. Magn Reson Imaging 1995;13(3):343–68.
[4] Gordillo N, Montseny E, Sobrevilla P. State of the art survey on MRI brain tumor segmentation. Magn Reson Imaging 2013;31(8):1426–38.
[5] Dora L, Agrawal S, Panda R, Abraham A. State-of-the-art methods for brain tissue segmentation: a review. IEEE Rev Biomed Eng 2017;10:235–49.
[6] Le Thi HA, Le HM, Dinh TP. Fuzzy clustering based on non-convex optimisation approaches using difference of convex (DC) functions algorithms. Adv Data Anal Classi 2007;1(2):85–104.
[7] Brown ES, Chan TF, Bresson X. Completely convex formulation of the Chan-Vese image segmentation model. Int J Comput Vision 2012;98(1):103–21.
[8] Vese LA, Chan TF. A multiphase level set framework for image segmentation using the Mumford and Shah model. Int J Comput Vision 2002;50(3):271–93.
[9] Pham DL, Prince JL. Adaptive fuzzy segmentation of magnetic resonance images. IEEE T Med Imaging 1999;18(9):737–52.
[10] Suckling J, Sigmundsson T, Greenwood K, Bullmore E. A modified fuzzy clustering algorithm for operator independent brain tissue classification of dual echo MR images. Magn Reson Imaging 1999;17(7):1065–76.
[11] Sikka K, Sinha N, Singh PK, Mishra AK. A fully automated algorithm under modified FCM framework for improved brain MR image segmentation. Magn Reson Imaging 2009;27(7):994–1004.
[12] Elazab A, Wang C, Jia F, Wu J, Li G, Hu Q. Segmentation of brain tissues from magnetic resonance images using adaptively regularized kernel-based fuzzy C-means clustering. Comput Math Method M 2015;2015. https://doi.org/10.1155/2015/485495. (12 pages).
[13] Namburu A, kumar Samay S, Edara SR. Soft fuzzy rough set-based MR brain image segmentation. Appl Soft Comput 2017;54:456–66.
[14] Lei T, Jia X, Zhang Y, He L, Meng H, Nandi AK. Significantly fast and robust fuzzy C-means clustering algorithm based on morphological reconstruction and membership filtering. IEEE T Fuzzy Syst 2018:1. https://doi.org/10.1109/TFUZZ.2018.2796074.
[15] Pham TX, Siarry P, Oulhadj H. Integrating fuzzy entropy clustering with an improved PSO for MRI brain image segmentation. Appl Soft Comput 2018;65:230–42.
[16] Vovk U, Pernus F, Likar B. A review of methods for correction of intensity inhomogeneity in MRI. IEEE T Med Imaging 2007;26(3):405–21.
[17] Jayadevappa D, Srinivas Kumar S, Murty D. Medical image segmentation algorithms using deformable models: a review. IETE Tech Rev 2011;28(3):248–55.
[18] Li C, Huang R, Ding Z, Gatenby JC, Metaxas DN, Gore JC. A level set method for image segmentation in the presence of intensity inhomogeneities with application to MRI. IEEE T Image Process 2011;20(7):2007–16.
[19] Liu L, Zhang Q, Wu M, Li W, Shang F. Adaptive segmentation of magnetic resonance images with intensity inhomogeneity using level set method. Magn Reson Imaging 2013;31(4):567–74.
[20] Li C, Gore JC, Davatzikos C. Multiplicative intrinsic component optimization (MICO) for MRI bias field estimation and tissue segmentation. Magn Reson Imaging 2014;32(7):913–23.
[21] Huang C, Zeng L. An active contour model for the segmentation of images with intensity inhomogeneities and bias field estimation. PloS One 2015;10(4):e0120399.
[22] Li X, Wang X, Dai Y. Adaptive energy weight based active contour model for robust medical image segmentation. J Signal Process Syst 2018;90(3):449–65.
[23] Mandal D, Chatterjee A, Maitra M. Robust medical image segmentation using particle swarm optimization aided level set based global fitting energy active contour approach. Eng Appl Artif Intel 2014;35:199–214.
[24] Chan TF, Vese LA. Active contours without edges. IEEE T Image Process 2001;10(2):266–77.
[25] Bong C-W, Rajeswari M. Multi-objective nature-inspired clustering and classification techniques for image segmentation. Appl Soft Comput 2011;11(4):3271–82.
[26] Mukhopadhyay A, Maulik U, Bandyopadhyay S. Multiobjective genetic clustering with ensemble among Pareto front solutions: application to MRI brain image segmentation. Proc ICAPR'09. IEEE; 2009. p. 236–9.
[27] Mukhopadhyay A, Maulik U. A multiobjective approach to MR brain image segmentation. Appl Soft Comput 2011;11(1):872–80.
[28] Zhao F, Liu H, Fan J. A multiobjective spatial fuzzy clustering algorithm for image segmentation. Appl Soft Comput 2015;30:48–57.
[29] Abdelaziz FB, Limam O. Multiobjective fuzzy clustering with coalition formation: the case of brain image processing. INFOR Inf Syst Oper Res 2017;55(1):52–69.
[30] Saha S, Bandyopadhyay S. Automatic MR brain image segmentation using a multiseed based multiobjective clustering approach. Appl Intell 2011;35(3):411–27.
[31] Zhang M, Jiao L, Ma W, Ma J, Gong M. Multi-objective evolutionary fuzzy clustering for image segmentation with MOEA/D. Appl Soft Comput 2016;48:621–37.
[32] Benaichouche AN, Oulhadj H, Siarry P. Multiobjective improved spatial fuzzy c-means clustering for image segmentation combining Pareto-optimal clusters. J Heuristics 2016;22(4):383–404.
[33] Eberhart R, Kennedy J. A new optimizer using particle swarm theory. Proc. MHS'95. IEEE; 1995. p. 39–43.
[34] Abubaker A, Baharum A, Alrefaei M. Automatic clustering using multi-objective particle swarm and simulated annealing. PloS one 2015;10(7):e0130995.
[35] Gong C, Chen H, He W, Zhang Z. Improved multi-objective clustering algorithm using particle swarm optimization. PloS one 2017;12(12):e0188815.
[36] Sierra MR, Coello CAC. Improving PSO-based multi-objective optimization using crowding, mutation and ϵ-dominance. Proc EMO'05. Springer; 2005. p. 505–19.
[37] Branke J, Mostaghim S. About selecting the personal best in multi-objective particle swarm optimization. Proc PPSN IX. Springer; 2006. p. 523–32.
[38] Zhang Y, Gong D-w, Cheng J. Multi-objective particle swarm optimization approach for cost-based feature selection in classification. IEEE ACM T Comput Bi

2017;14(1):64–75.
[39] Padhye N, Deb K. Multi-objective optimisation and multi-criteria decision making in SLS using evolutionary approaches. Rapid Prototyping J 2011;17(6):458–78.
[40] Kwan R-S, Evans AC, Pike GB. MRI simulation-based evaluation of image-processing and classification methods. IEEE T Med Imaging 1999;18(11):1085–97.
[41] Zhang Y-D, Zhang Y, Lv Y-D, Hou X-X, Liu F-Y, Jia W-J, et al. Alcoholism detection by medical robots based on Hu moment invariants and predator–prey adaptive-inertia chaotic particle swarm optimization. Computers and Electrical Engineering 2017;63:126–38.
[42] Zhang Y, Wang S, Sui Y, Yang M, Liu B, Cheng H, et al. Multivariate approach for Alzheimer's disease detection using stationary wavelet entropy and predator-prey particle swarm optimization. J Alzheimers Dis 2018;65(3):855–69.
[43] Reyes-Sierra M, Coello CAC. Multi-objective particle swarm optimizers: a survey of the state-of-the-art. IJCIR 2006;2(3):287–308.
[44] Paoli A, Melgani F, Pasolli E. Clustering of hyperspectral images based on multi-objective particle swarm optimization. IEEE T Geosci Remote 2009;47(12):4175–88.
[45] Arulraj M, Nakib A, Cooren Y, Siarry P. Multicriteria image thresholding based on multiobjective particle swarm optimization. Appl Math Sci 2014;8(3):131–7.
[46] Deb K, Pratap A, Agarwal S, Meyarivan T. A fast and elitist multiobjective genetic algorithm: NSGA-II. IEEE Transactions on Evolutionary Computation 2002;6(2):182–97.
[47] Knowles JD, Corne DW. Approximating the nondominated front using the Pareto archived evolution strategy. Evol Comput 2000;8(2):149–72.
[48] Lee J-M, Yoon U, Nam SH, Kim J-H, Kim I-Y, Kim SI. Evaluation of automated and semi-automated skull-stripping algorithms using similarity index and segmentation error. Comput Biol Med 2003;33(6):495–507.
[49] Chabrier S, Emile B, Laurent H, Rosenberger C, Marche P. Unsupervised evaluation of image segmentation application to multi-spectral images. Proceedings of the 17th International Conference on Pattern Recognition, 2004. ICPR 2004. vol. 1. IEEE; 2004. p. 576–9.
[50] Chabrier S, Emile B, Rosenberger C, Laurent H. Unsupervised performance evaluation of image segmentation. EURASIP Journal on Applied Signal Processing 2006(2006):1–12.
[51] Borsotti M, Campadelli P, Schettini R. Quantitative evaluation of color image segmentation results. Pattern recognition letters 1998;19(8):741–7.
[52] Buades A, Coll B, Morel J-M. A non-local algorithm for image denoising. 2005 IEEE Computer Society Conference on Computer Vision and Pattern Recognition (CVPR'05). vol. 2. IEEE; 2005. p. 60–5.
[53] Sethian J. Level set methods and fast marching methods. Cambridge: Cambridge University Press; June 1999.
[54] Li C, Xu C, Gui C, Fox MD. Level set evolution without re-initialization: a new variational formulation. Proc IEEE Conf Comput Vis Pattern Recognit (CVPR). vol. 1. IEEE; 2005. p. 430–6.
[55] Wang L, Li C, Sun Q, Xia D, Kao C-Y. Active contours driven by local and global intensity fitting energy with application to brain MR image segmentation. Comput Med Imag Grap 2009;33(7):520–31.
[56] Wang X-F, Huang D-S, Xu H. An efficient local Chan–Vese model for image segmentation. Pattern Recogn 2010;43(3):603–18.
[57] Zhao L, Zheng S, Wei H, Gui L. Adaptive active contour model driven by global and local intensity fitting energy for image segmentation. Optik 2017;140:908–20.
[58] Wang Z, Rangaiah GP. Application and analysis of methods for selecting an optimal solution from the Pareto-optimal front obtained by multiobjective optimization. Ind Eng Chem Res 2017;56(2):560–74.
[59] Krishnan PT, Balasubramanian P, Krishnan C. Segmentation of brain regions by integrating meta heuristic multilevel threshold with Markov random field. Current Medical Imaging Reviews 2016;12(1):4–12.
[60] Li C, Kao C-Y, Gore JC, Ding Z. Minimization of region-scalable fitting energy for image segmentation. IEEE T Image Process 2008;17(10):1940–9.
[61] Lankton S, Tannenbaum A. Localizing region-based active contours. IEEE T Image Process 2008;17(11):2029–39.
[62] Foster B, Bagci U, Mansoor A, Xu Z, Mollura DJ. A review on segmentation of positron emission tomography images. Comput Biol Med 2014;50:76–96.
[63] Dice LR. Measures of the amount of ecologic association between species. Ecology 1945;26(3):297–302.
[64] Beauchemin M, Thomson KP, Edwards G. On the Hausdorff distance used for the evaluation of segmentation results. Can J Remote Sens 1998;24(1):3–8.
[65] Jaccard P. The distribution of the flora in the alpine zone. New Phytol 1912;11(2):37–50.
[66] Taha AA, Hanbury A. Metrics for evaluating 3D medical image segmentation: analysis, selection, and tool. BMC Med Imaging 2015;15(1):29.